The evolution of subsurface deformation and tribological degradation of a multiphase Fe-based hardfacing induced by sliding contact

M.J. Carrington [a,d,*], J.L. Daure [a], S. Utada [c], V.L. Ratia-Hanby [a,e], P.H. Shipway [a], D.A. Stewart [b], D.G. McCartney [a]

[a] *Advanced Materials Group, Faculty of Engineering, University of Nottingham, Nottingham, NG7 2RD, UK*
[b] *Rolls-Royce plc, UK*
[c] *Department of Materials, University of Oxford, Parks Road, Oxford, OX1 3PH, UK*
[d] *Applied Materials Technology group, UK Atomic Energy Authority, Culham Science Centre, Abingdon, Oxfordshire, OX14 3DB, UK*
[e] *VTT Technical Research Centre of Finland Ltd, P.O. Box 1000, FI-02044 VTT, Finland*

ARTICLE INFO

ABSTRACT

Multiphase Fe-based hardfacing alloys, for example Tristelle 5183 Fe-21%Cr-10%Ni-7.5%Nb-5%Si-2%C in wt.%, are extensively used for tribological applications, including valves, bearings and drive mechanisms, where two surfaces are unavoidably subjected to loaded sliding contact within engineering systems. In this study, transmission electron microscopy (TEM), scanning electron microscopy (SEM), and X-ray diffraction (XRD) were used to characterise, for the first time, the tribologically affected material induced by the self-mated sliding contact of HIPed Tristelle 5183. This provided novel insight into the deformation modes which permit the accumulation of the high levels of subsurface strain required for plasticity dominated (adhesive) wear in a commercial hardfacing. In the subsurface regions furthest from the sliding contact, plastic deformation is accommodated by deformation induced martensitic transformation to ϵ-martensite and $\alpha\prime$-martensite, twinning, the generation of planar dislocation arrangements (generated by planar slip) and the generation of dislocation tangles. Closer to the sliding contact, the subsurface becomes unstable, and nanocrystallisation driven by grain boundary mediated deformation mechanisms and crystallographic slip completely engulf the near surface microstructure. It is postulated that nanocrystalisation within the subsurface is a needed in order to accommodate the extremely high strains required in order to permit tribological degradation via plasticity dominated wear. The extrusion of metallic slivers via plastic ratcheting generates ductile shear cracks governed by plastic strain, and the failure of these slivers generates plate/flake-like wear debris.

1. Introduction

Understanding the plastic deformation mechanisms which govern microstructural evolution in response to the sliding contact between two surfaces is fundamentally important when evaluating the tribological degradation mechanisms of an alloy. The unique loading conditions generated during sliding contact, and the resulting high hydrostatic component of stress, mean that materials are often subjected to extremely high strains prior to tribological failure/degradation. This seemingly ductile response to sliding contact is also observed in hardfacing alloys containing secondary hard phase precipitates embedded in a ductile metal matrix, which would otherwise fail with little ductility when subjected to other loading conditions. In the case of many alloys and hardfacings, the accumulation of enormous subsurface strains during sliding leads to surface failure by a degradation mode more generally termed plasticity dominated or adhesive wear. There exist many

wear theories which provide elaborate descriptions of the mechanisms of material removal during plasticity dominated wear [1–6]. Nevertheless, there is a lack of experimental evidence for these theoretical descriptions; moreover, they do not generally elucidate and/or conclusively explain the deformation modes and microstructural evolution which permits the accommodation of the large strains required for such wear.

Significant progress has been made using transmission electron microscopy (TEM) to examine the subsurface deformation microstructures generated by sliding [7,8]. However, given the complexity of deformed microstructures induced by sliding contact, this work has generally been confined to the investigation of single phase alloys, particularly those which with a reportedly high stacking fault energy (SFE ($\gtrsim$ 40 mJ/m^2)). The deformation structures and subsequent work hardening behaviours of austenitic stainless steels are fundamentally dependent upon their stacking fault energy (SFE) which is

---

influenced by both temperature and composition [9,10]. As the SFE decreases, the plastic deformation mechanisms for austenitic steels shift from dislocation glide and climb (high SFE), to dislocation glide and climb plus mechanical twinning, to dislocation glide and climb plus martensitic transformation (low SFE) [9–16]. The present work seeks to understand the deformation mechanisms and microstructural evolution which permits plasticity dominated wear in the low SFE ($\lesssim 18$ mJ/m^2) multiphase Fe-based hardfacings which are more commonly used in industrial applications, including valves, bearings, and drive mechanisms. Tristelle 5183 (Fe-21%Cr-10%Ni-7.5%Nb-5%Si-2%C in wt.%) is one such hardfacing alloy which has received particular attention in recent years [17–26], particularly within the nuclear industry, because it is a corrosion resistant Fe-based alternative to the more expensive Co-based Stellite family of hardfacing alloys (Co-Cr-Si-W-C type alloys). It is also desirable to replace Stellite with Co-free materials in order to avoid problems with ^{59}Co debris being transmuted to the γ-emitting isotope ^{60}Co (half-life: ~5.3 years) which is a major source of radiation exposure for plant and maintenance workers [27,28].

The present work looks at Tristelle 5183 manufactured by powder hot isostatic pressing (HIPing) of gas atomised feedstock. Traditional hardfacing techniques, namely those reliant on solidification from the liquid or partially liquid state, for example, weld overlay or laser cladding [29], inherently suffer from performance compromising defects such as pores, cracks, and dilution with the substrate. Given the safety critical nature of many engineering components requiring hardfacing, the production of hardfacings by powder HIPing is often the manufacturing route of choice for hardfaced components. The advantages of powder HIPing including better chemical and microstructural homogeneity and fewer defects compared to more traditional methods of hardfacing [30].

In light of the above, its is clear that there is need for a greater understanding of the subsurface deformation modes that permit the activation of plasticity dominated wear during the sliding contact of HIPed Fe-based hardfacings. The paucity of information significantly inhibits the development of wear theories which mechanistically describe the plasticity dominated wear of Fe-based hardfacing from first principles, without simply assuming that the subsurface can readily accommodate enormous strains. Such a wear theory would be pivotal in the development of new Fe-based hardfacings which exhibit a greater resistance to plasticity dominated wear. In this study, water-lubricated, self-mated pin-on-disc type wear tests were conducted on HIPed Tristelle 5183, and the tribologically affected material was investigated by techniques including X-ray diffraction, scanning electron microscopy, and transmission electron microscopy. The aim of this work was to elucidate the following key points: (i) the subsurface microstructural evolution and deformation modes ; (ii) The relationship between deformation modes and strain distribution beneath the sliding contact; and (iii), the sub-surface deformation structures which permit surface failure by plasticity dominated wear.

2. Materials and methods

2.1. Materials

Tristelle 5183 powder (nominal composition: Fe-21%Cr-10%Ni-7.5%Nb-5%Si-2%C in wt.%) was manufactured using nitrogen gas atomisation to give a near-spherical powder particle morphology with a particle size typically < 500 μm. The chemical composition of this powder is reported in Table 1 and was measured using inductively coupled plasma (ICP) spectrometry and Leco combustion analysis for the measurement of carbon and nitrogen. The powder was classified into 60–150 μm sized powder particles and HIPed into bar form (30 mm ø × 200 mm) using mild steel canisters at 1120 °C ± 10 K and 103 MPa ± 5 MPa with a dwell time of 240–270 min and a cooling rate of 3.4–5.5 K/min.

Table 1

Chemical composition of (60–150 μm) Tristelle 5183 powder as determined by ICP and combustion analysis.

| | Element % | | | | | | | |
	Fe	Cr	Ni	Nb	Si	C	N	Other
wt%	Bal.	21.72	10.39	6.90	4.67	2.08	0.05	0.73
at%	Bal.	21.07	8.93	3.75	8.40	8.75	0.17	0.63

2.2. Sliding contact water lubricated wear testing

Pin-on-disc type wear testing was conducted at room temperature (~20 °C) using a bespoke tribometer which allowed testing to be conducted within an aqueous environment. The full details of the wear tests are given elsewhere [31–33]. The sliding contact test apparatus was immersed in deoxygenated deionised water with the addition of 8.5 mg LiOH per litre which was used in order to simulate the water chemistry of a primary circuit of a PWR. This environment has recently attracted particular attention within the literature [18,31–37], and is one within which corrosion resistant Fe-based multiphase hardfacings are used. The pin and disc samples were machined via EDM and the (contacting) surfaces were surface ground to an Ra of ~0.4 μm. The cylindrical pins were machined to a 10 mm diameter and a 50 mm radius spherical end cap was ground onto the testing surface, whereas the discs were 30 mm in diameter with parallel ground end faces. The disc was secured in a rotating sample holder and the pin was uniaxially loaded against the rotating disc, 10 mm from the disc's axis of rotation, through the application of a 4 kg dead load. A constant rotational speed of 200 rpm was applied for a 5 h duration resulting in a total mean sliding distance of ~3770 m.

2.3. Materials characterisation

Bulk metallurgical and cross-sectional wear samples were initially machined via electrical discharge machining (EDM) or using a cubic boron nitride cut-off wheel. These samples were subsequently ground, diamond polished to a 1 μm finish, and then given a final polish using 0.06 μm colloidal silica prior to analysis by X-ray diffraction (XRD) and microstructural analysis in a scanning electron microscope (SEM). Backscattered electron (BSE) and secondary electron (SE) SEM imaging of the polished samples and worn surface samples was performed on a tungsten filament FEI Quanta 600 operating at 20 kV. EBSD data from polished samples were acquired using a Jeol 7100F field emission gun SEM (FEG-SEM) operating at 15 kV equipped with a Oxford Instruments Nordlys Nano EBSD detector. Micro-hardness measurements were performed using a Buehler MMT-7 Digital Micro-Hardness tester employing a Knoop indenter and a 25 gf load.

X-ray difractograms of the alloy and tribologically affected surfaces were recorded using a Bragg–Brentano (θ-θ) configured Bruker D8 employing Cu K-α radiation and a LYNXEYE XE-T position sensitive (1D) energy discriminating detector. This machine is equipped with a variable anti-scatter screen, variable divergent slits, and a variable detector window. It was operated with a working voltage and current of 40 kV and 40 mA respectively. Scans were performed with a step size of 0.02° between 20 and 120° 2θ. Rietveld refinements [38] were performed using Topas V6 software (Bruker) and the fundamental parameters approach to X-ray line profile fitting was employed [39,40].

Electron transparent transmission electron microscope (TEM) lamellae (50–120 nm in thickness) were prepared from regions near the surface of the wear tracks of disc samples using an FEI Scios DualBeam. A standard focused ion beam (FIB) liftout method was employed [41]. TEM lamellae aligned parallel to the sliding direction and perpendicular to the worn surface were taken from the centre of wear tracks. Lamellae procured from 60 μm beneath the sliding contact were extracted from polished cross-sectioned samples. Prior to FIB lift out platinum was deposited by electron beam onto the worn surface to
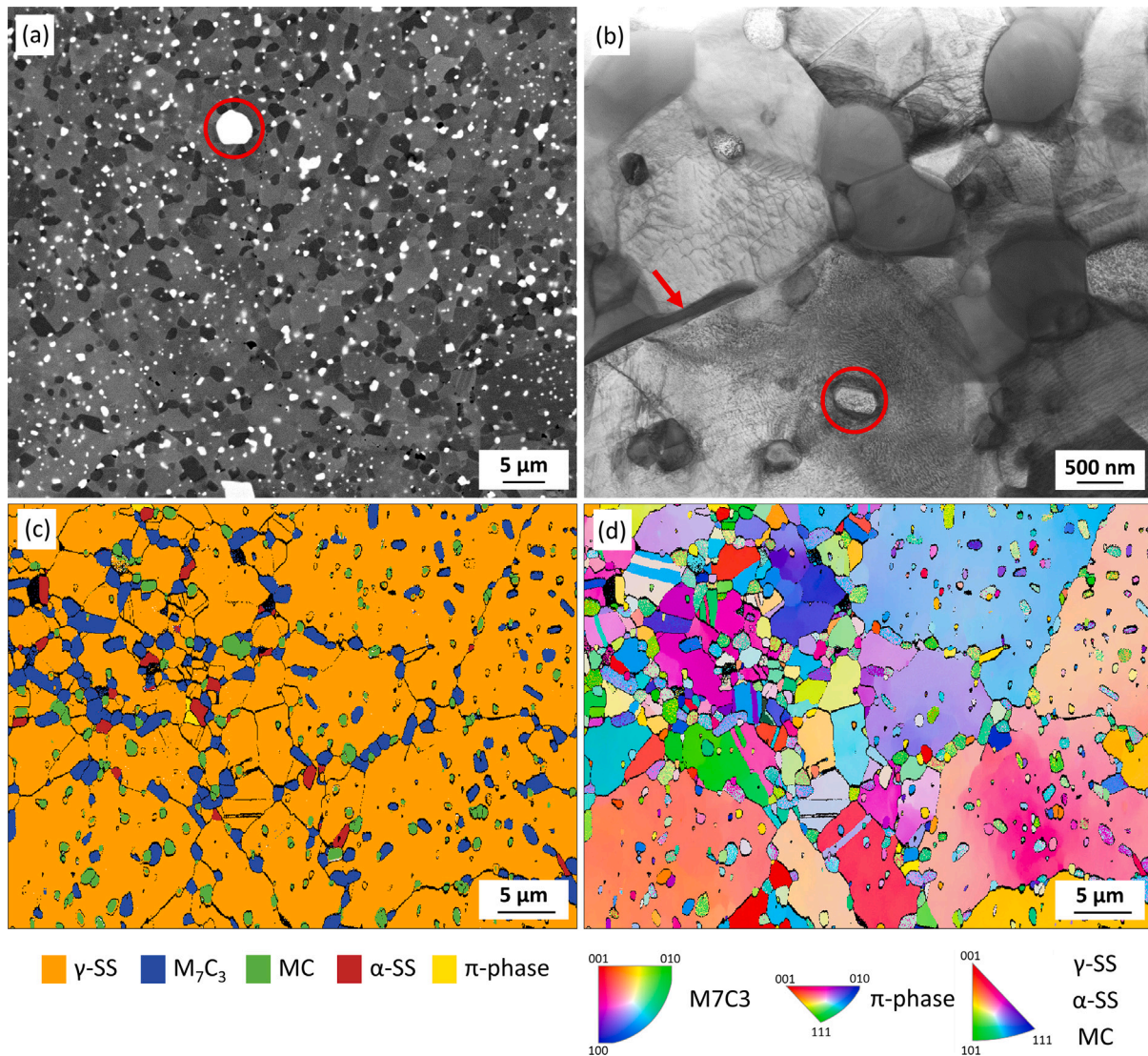
Fig. 1. BSE-SEM micrograph (a), STEM micrograph (b) and both EBSD-derived phase (c) and IPF (d) maps of HIPed Tristelle 5183. (For interpretation of the references to colour in this figure legend, the reader is referred to the web version of this article.)

protect against FIB induced surface damage. Conventional bright field (BF), dark field (DF) and selected area electron diffraction (SAED) was conducted using a JEOL 2100+ operating at 200 kV. Scanning transmission electron microscopy (STEM) and EDX were undertaken using a FEG source FEI Talos F200X TEM operating at 200 kV.

3. Results

3.1. Characterisation of as-received alloy

A detailed characterisation of the microstructure of the alloy and its formation during gas atomisation and powder HIPing is given in Refs. [31,42]. Nevertheless, a brief summary is required here as a baseline microstructure in order to elucidate the tribologically induced microstructural evolution.

Fig. 1 shows a BSE-SEM micrograph (a), a STEM micrograph (b) and EBSD derived phase maps (c) and inverse pole figure (IPF) maps (d) of the representative microstructure of the as-received alloy. The Fe-based matrix and secondary hard phase precipitates are distinguishable in the BSE-SEM micrographs and can be related to the phases identified by EBSD. The Fe-based matrix and secondary hard phase precipitates can be distinguished in the BSE-SEM micrographs and related to the

phases identified by EBSD. The volume fractions of the phases in the as-received material were evaluated using Rietveld and EBSD to be 74%–76% γ-Fe, 13%–14% M_7C_3, 10%–11% MC, 1%–2% α-Fe solid solution and $< 1\% \pi$-ferrosilicide in vol.%

The matrix is a γ-Fe solid solution (Fig. 1(c)), and SEM-EDX evaluated its composition as 60.0 ± 0.2%Fe-16.2 ± 0.1%Cr-11.3 ± 0.1%Ni-11.6 ± 0.1%Si-0.9 ± 0.2% other in at.% (mean ± standard error of the mean (n = 6)). The IPF map reveals a range of grain sizes and the variation is believed to develop during the HIP consolidation of powder [42].

The dark-contrast features ~1–5 μm in size (Fig. 1(a) and (b)) are the Cr-rich M_7C_3 (~$(0.82Cr0.18Fe)_7C_3$) carbides (basic structure in the Pmcn space group) identified by EBSD (blue precipitates in (Fig. 1(c)). The bright-contrast precipitates in Fig. 1(a) are the Nb-rich (MC) fcc phase identified by EBSD (green particles in Fig. 1(c)). The MC phase clearly has a bimodal precipitate size distribution [42] which arises from the gas atomisation stage of manufacturing as explained in Ref. [31]. This bimodal distribution can be characterised by the following: (i) spheroidised MC precipitates <2 μm accounting for approximately 70 vol.% of the MC phase; and (ii), larger 5–20 μm sized precipitates (red circle in Fig. 1(a)) which account for the reaming fraction of MC phase (30 vol.%).
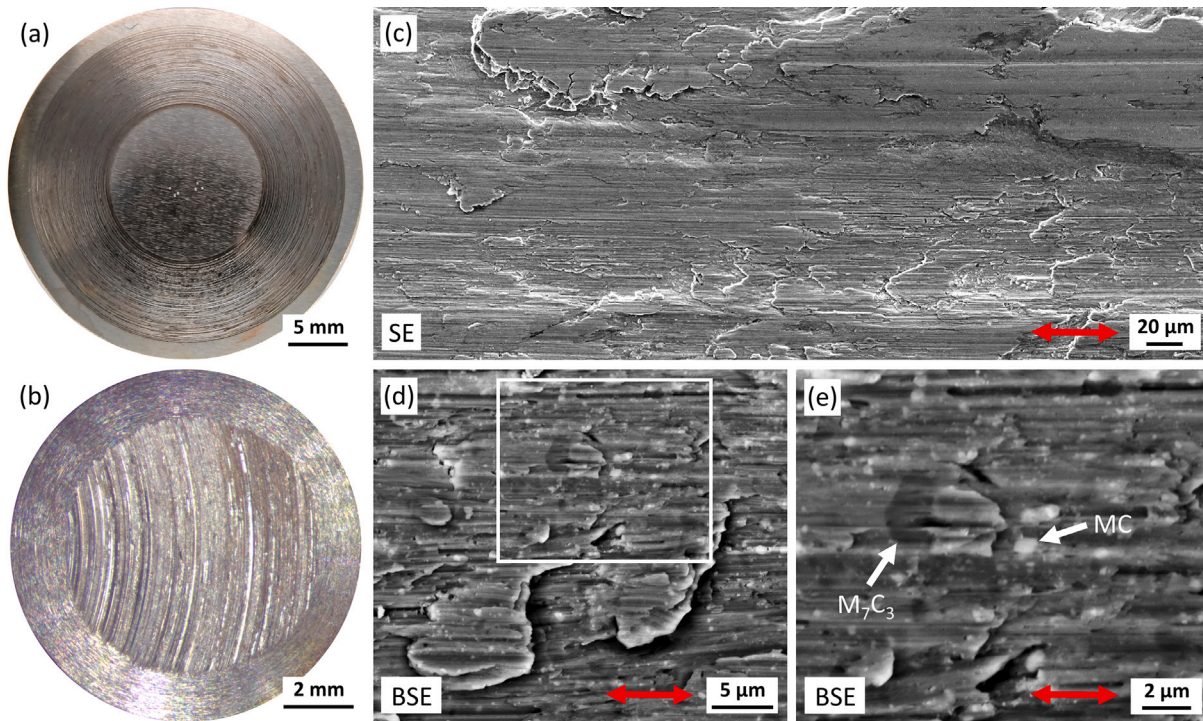
Fig. 2. Stereoscope optical micrographs of disc (a) and pin (b) tribologically affected surfaces following water lubricated sliding contact tests. SE (c) and BSE (d and e) SEM micrographs showing the tribologically affected surface of a disc sample after water lubricated sliding contact tests. (e) is a higher magnification image of the region marked with the white square in (d). The sliding direction is indicated by the red arrows.

Smaller fractions of ferrite and a π-ferrosilicide phase (isostructural to $Fe_5Ni_3Si_2$ and $Cr_3Ni_5Si_2$ (P2$_1$3)) have also been identified by EBSD (Fig. 1(c)) and TEM (red arrow in Fig. 1(b)). Both of these phases are typically <2 μm in size and account for <3 vol.% of the total alloy.

3.2. Topography of the worn surface and wear behaviour

Fig. 2(a) and (b) show low magnification optical micrographs of representative disc (Fig. 2(a)) and pin (Fig. 2(b)) tribologically affected surfaces after testing. Both of these worn surfaces exhibit features characteristic of adhesive (plasticity dominated) wear [43]. Generally, the mechanisms of degradation are similar for both the pin and disc; thus, only results obtained from disc samples will be reported hereafter. The disc wear track (Fig. 2(a)) measures ~6.9 mm in width. Likewise, the maximum average wear track depth was evaluated by profilometry to be ~11 μm.

The mean specific wear rate of Tristelle 5183 was found to be 34.2 ± 3.9 × 10^{-6} mm^{3}m^{-1}N^{-1} (density = 7505 kg/m3). As reported in a previous paper, this is significantly more than Stellite 6 (widely used in PWR environments) which had a specific wear rate of 1.17 × 10^{-6} mm^{3}m^{-1}N^{-1} under identical sliding conditions [34].

Fig. 2 shows plan view SE (Fig. 2(c)) and BSE (Fig. 2(d) and (e)) micrographs from central regions within a wear track (sliding direction indicated by red arrows). The worn surface shows features that are characteristic of plasticity dominated wear with highly deformed slivers/platelets of material. Extruded slivers which have incurred gross plastic deformation are extensively observed within the wear track and are clearly elongated in the sliding direction. In some instances, there is discontinuity between the extruded slivers and underlying material in the form of ductile shear cracks. This makes the slivers appear partially delaminated. The bright and dark contrast precipitates visible in the BSE micrographs (Fig. 2(d) and (e)) are the Nb-based MC and Cr-based M_7C_3 carbide phases respectively which were previously been identified in the as-received material (Fig. 1).
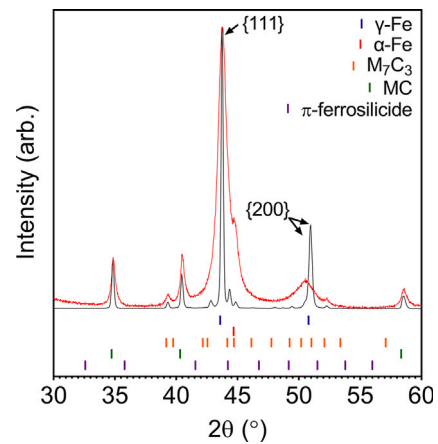

Fig. 3. XRD patterns of HIPed Tristelle 5183 in the polished as-received condition (black) and from within the central region of a wear track (red). Patterns normalised to the {111} reflection of maximum intensity. (For interpretation of the references to colour in this figure legend, the reader is referred to the web version of this article.)

3.3. XRD of tribologically affected material

The X-ray diffractograms shown in Fig. 3 were obtained from polished as-received material (black) and from the surface of a wear track (red). The phases observed in the diffractograms from the as-received material were also identified by EBSD (Fig. 1). The volume fractions of the phases in the as-received alloy were determined by Rietveld analysis of XRD patterns as 74%–76% γ-Fe, 13%–14% M_7C_3, 10%–11% MC, 1%–2% α-Fe solid solution and < 1%π-ferrosilicide in vol.%.

Even though the X-ray intensity contributing to the diffracted signal decreases exponentially with increasing depth into the sample [44], the average X-ray penetration depth contributing 99% of the diffracted intensity was on average ~4 μm over the range of 2θ values (30–60°) used
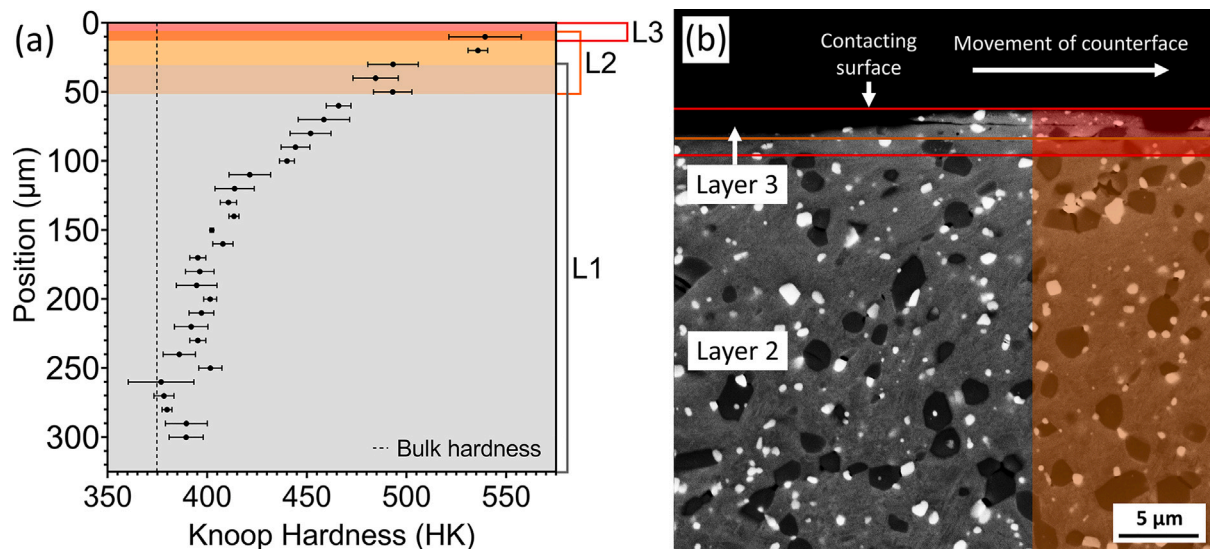
Fig. 4. (a) Microhardness (10 g load) profile taken from a perpendicular cross sections of a wear track following water lubricated sliding contact. The errors have been reported as the standard error of the mean. The three overlapping layers, designated L1 (grey shading), L2 (orange shading) and L3 (red shading), represent the different layers within the TAM used to describe the continuum of plastic deformation within the subsurface. Likewise, (b) shows a BSE micrograph showing the tribologically affected regions corresponding to layer 2 (orange shading) and layer 3 (red shading). (For interpretation of the references to colour in this figure legend, the reader is referred to the web version of this article.)

in the XRD measurements of the tribologically affected surface [44]. These diffractograms have an additional contribution from reflections consistent with bct $\alpha\prime$-Fe which overlap with the peaks for bcc α-Fe (e.g., at $\sim 44.8°$). This is therefore observed as a relative increase in the α-Fe reflections compared to those observed in the as-received material. The $\alpha\prime$-Fe is observed due to the deformation induced martensitic (DIM) transformation of the γ-Fe matrix which is expected to have a low SFE ($\lesssim 20$ mJ/m^2). With reference to the peak shapes of all the phases, the pattern from the wear track is significantly different to that of the as-received material; moreover, these changes in peak shape are a result of crystallographic faulting and crystallite size and strain broadening effects induced by sliding contact.

The γ-Fe reflections are particularly sensitive to modification following tribological testing, and profound differences concerning the peak broadening, maximum peak intensities, peak shift, and peak asymmetry of the γ-Fe reflections are observed between the polished and worn surfaces. Firstly, tribological testing clearly causes a broadening of the γ-Fe reflections, and this broadening is particularly noticeable in the {200} reflection. Secondly, there is a notable difference in the peak height ratios of the {111} : {200} γ-Fe reflections in the diffractogram following wear testing compared to the polished sample. Finally, there is a significant shift of the {200} reflection towards lower 2θ values following testing relative to the polished sample. These phenomena are all believed to be due to a number of factors including, crystallographic flaws (stacking faults), crystallite size and microstrain broadening and a possible contribution from a sliding induced preferred orientation of the {111} parallel to the sliding direction (tribologically affected surface).

3.4. Sub-surface microstructural classification

The tribologically affected material (TAM) beneath a worn surface is often described as a continuum of deformation which results from a sliding induced strain gradient where the highest strains are generated at the contacting interface [43]. Nevertheless, for the purpose of detailing the results, it is convenient to sub-divide the results of the TAM into three layers, termed L1 (layer 1) remote from the surface, L2 (layer 2) and L3 (layer 3), as schematically illustrated in Fig. 4. Fig. 4(a) shows a Knoop hardness profile from a perpendicular cross section of a wear track. This shows the extent of hardening as a function of depth beneath the contacting surface and is also illustrative of the variation in strain and/or plastic deformation with respect the depth

beneath the contacting surface. In other words, it is key to note that the hardness increase is a good proxy for subsurface strain. The immediate subsurface region (within the top 50 μm) shows a Knoop hardness that is 100 to 150 HK greater than that of the bulk alloy. This indicates that there must be a significant variation in microstructure with depth and the following sections will elucidate the details of these changes.

3.5. Nanocrystallisation and microstructural features of deformation — Layers 2 and 3

Cross-sectional BSE-SEM micrographs taken from within the wear track parallel to the sliding direction are shown in Fig. 5, and (b) shows the microstructural detail of the region marked in (a). Fig. 5(a) is an overview of the transition from layer 2 (L2) to layer 3 (L3), and (b) and (c) reveal more detail of the microstructural features approximately 20 and 4 μm from the contact surface respectively. The matrix microstructure below the surface has undergone considerable microstructural refinement due to severe plastic deformation and reveals a clear deformation gradient. The deformed microstructure contains elongated structures of varying contrast which tend to become aligned parallel to the sliding direction (Fig. 5(a) and (c)) in the regions near the contacting surface; clearly defined matrix grain boundaries are no longer easily distinguishable. This matrix has clearly incurred a highly localised deformation. A white dashed line in Fig. 5(a) and (c) (termed a displacement line by Dautzenburg et al. [45]) indicates the flow of the material based upon observations of microstructural features. Adapting the method proposed by Dautzenburg et al. [45,46], it is estimated from Eq. (3.1) that the strain in the upper regions of layer 2 must be of the order of 3. This value is in accord with values reported by others in the literature.

$$\epsilon = \frac{\tan(\theta)}{\sqrt{3}} \qquad (3.1)$$

Fig. 5(a) and (c) depict features representative of layer 3 and show extruded slivers/layers of grossly deformed material at the contacting interface which are principally composed of heavily mixed matrix (grey contrast) and whole or fractured MC (bright white contrast) and M_7C_3 (dark contrast) carbides. There is some evidence that MC particles tend to undergo fracture whereas M_7C_3 tends to exhibit wear-induced flat spots (red arrow in (a)). The generation of extruded features at the contacting surface is consistent with plasticity dominated wear and the
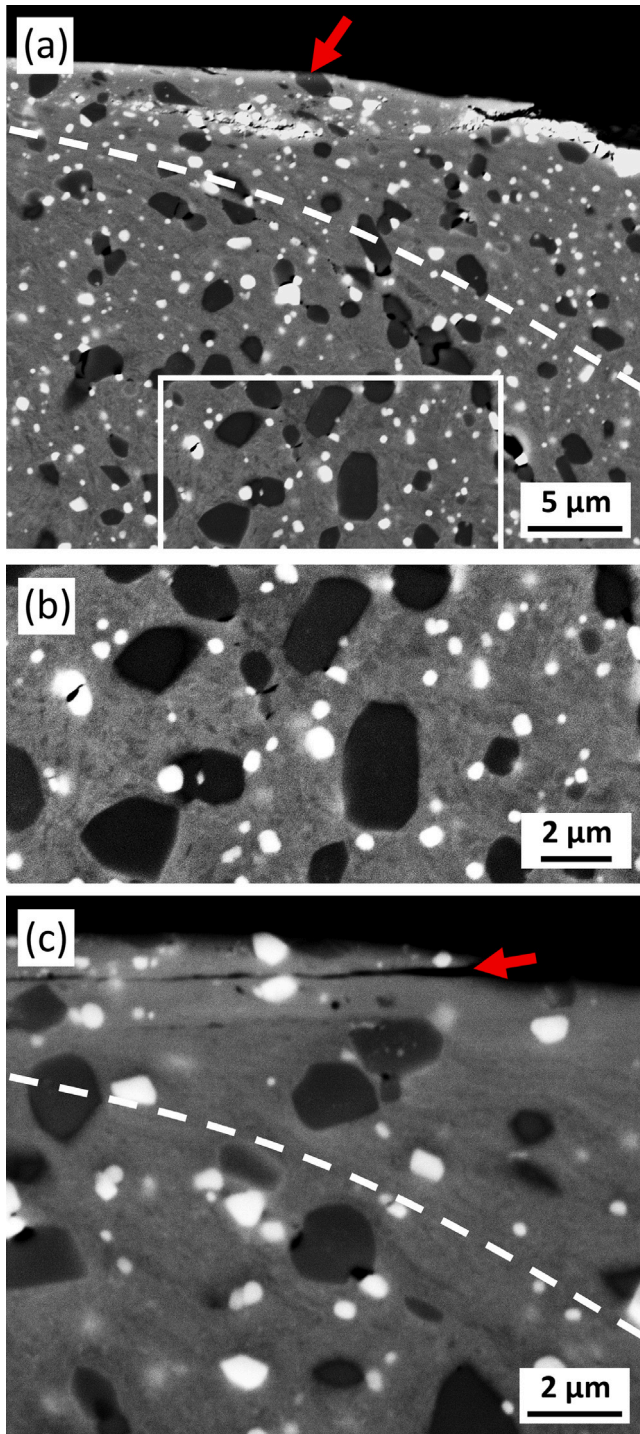
Fig. 5. (a) shows a cross-sectional BSE-SEM micrograph of Tristelle 5183 taken from within the wear track (parallel to the sliding direction) after water lubricated sliding contact testing. The M_7C_3 (dark contract) and MC (bright contrast) precipitates are distributed in a heavily deformed Fe-rich matrix. (b) shows a higher magnification image of the region marked with the white rectangle in (a). (c) is a BSE-SEM micrograph depicting extruded slivers/platelets of metallic material at the contacting interface. The sliding direction is horizontal to the figure in all cases.

surface regions identified by plan view SEM (Fig. 2). Fig. 5(c) shows a region of discontinuity in the form of a ductile shear crack between two extruded slivers which are approximately 1 μm in thickness (red arrow in (c)). This ductile shear crack is seemingly formed by extrusion and makes the uppermost sliver appear partially delaminated.
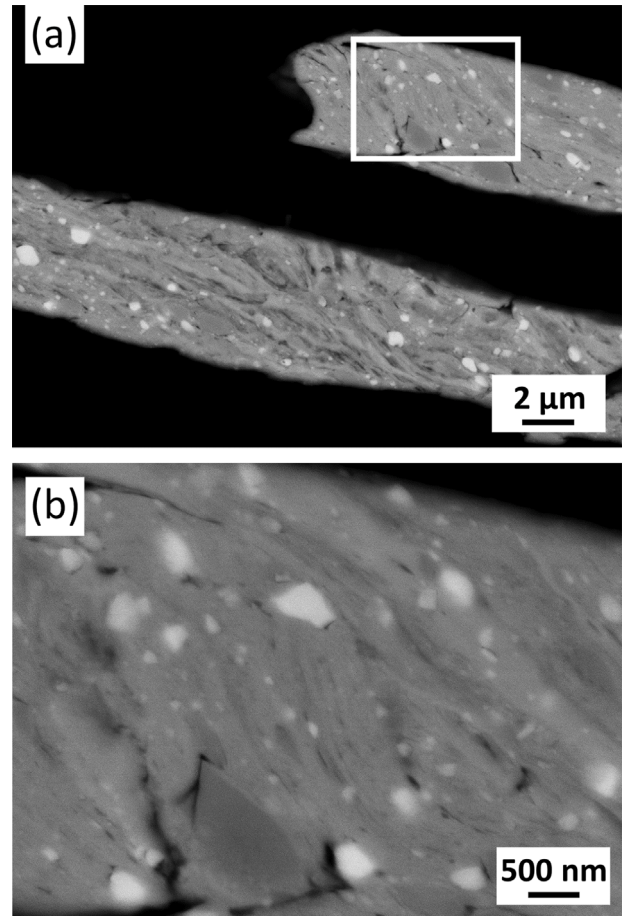

Fig. 6. Cross-sectional BSE-SEM channelling contrast micrographs of Tristelle 5183 plate-like wear debris retrieved after water lubricated sliding contact testing. (b) is a higher magnification image of the region marked with the white square in (a).

Fig. 6(a) and (b) show cross-sectional BSE images of plate/sliver like wear debris retrieved following tribological testing. This debris is consistent with the extruded slivers observed at the contacting surface in Fig. 2 and Fig. 5(a and c) and suggests that debris generation principally arises from the detachment of the extruded slivers. Likewise, the microstructure within the debris is principally composed of elongated structures/crystallites of varying contrast which are generally aligned parallel to the direction shear (along the length of the debris). In some regions within the debris, fine networks of cracks are observed which are different to the larger ductile shear cracks observed in Fig. 5(f). They are possibly fatigue cracks which may be associated with the final detachment of the extruded slivers.

The HAADF-STEM micrographs Fig. 7(a and b) have been taken parallel to the sliding direction and show the tribologically affected material up to ~5 μm below the contacting surface. The accompanying EDX maps (Fig. 7(c–h)) show the same region as Fig. 7(a). Fig. 7(a and b) depict a mechanically refined nanocrystalline matrix with embedded bright and dark contrast precipitates which are Cr-rich M_7C_3 (Fig. 7(d)) and Nb-rich MC (Fig. 7(e)) carbides respectively. Fig. 7(a) and (c–h) can be separated in to two distinctly different regions, namely: (i) layer 3 extending to a depth of ≲ 3 μm from the surface composed of overlapping extruded slivers/striations which contain whole and fractured carbides (Fig. 7 (d and e)); and (ii), a highly deformed region of material at a depth ≳ 3 μm from the surface representative of layer 2. The extruded slivers, representative of the features observed within layer 3, are highly coherent with one another and are best revealed in the EDX maps. However, the uppermost two slivers are clearly identifiable by small ductile shear cracks which form between their interfaces
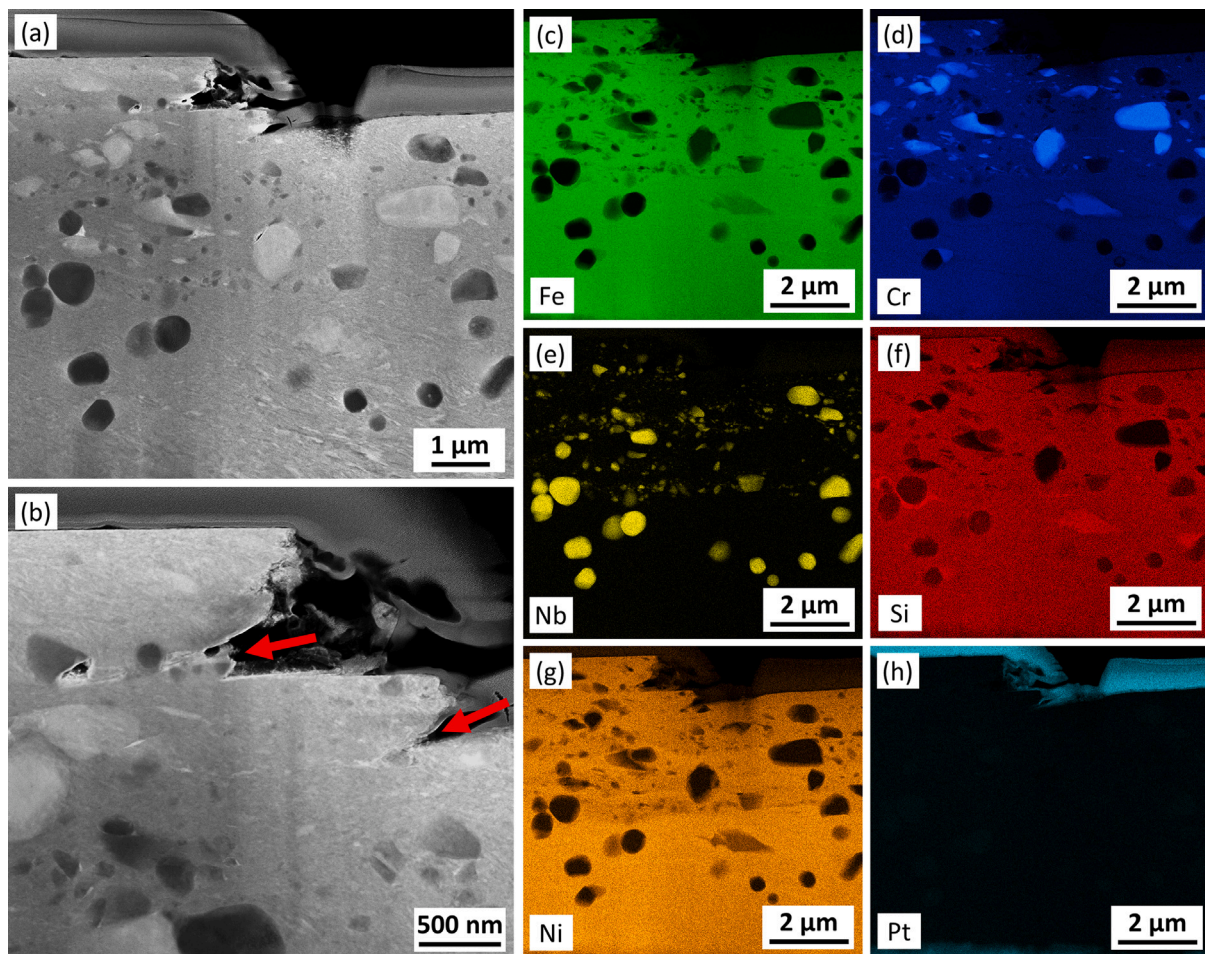
Fig. 7. (a) and (b) show representative HAADF-STEM micrographs taken parallel to the sliding direction showing the deformation structures directly beneath the contacting surface. (c), (d), (e), (f), (g) and (h) show EDX maps of the same region depicted in (a) and correspond to the maps for Fe, Cr, Nb, Si, Ni and Pt respectively. The sliding direction is horizontal to the figure in all cases.

(red arrows in Fig. 7(b)). Relative to the M_7C_3 carbide (Fig. 7(d)), the MC carbide (Fig. 7(e)) appears more susceptible to fragmentation during sliding. A large fraction of the fragmented carbides are isolated and surrounded by matrix material. This is presumably due to the high degree of mechanical mixing that occurs during sliding. The highly deformed matrix material is nanocrystalline and contains high aspect ratio crystallites (generally aligned parallel to the shear direction) which increasingly become more equiaxed closer to the contacting surface. This nanocrystalline microstructure would lead to the high Knoop hardness measured in this region of the TAM. In addition to carbides, the EDX maps also reveal deformed π-ferrosilicide precipitates (rich in Cr and Si and depleted in Ni and Fe relative to the matrix) which were observed in the as-received alloy Fig. 1.

Fig. 8(a–e) show BF-TEM micrographs depicting the fine detail of the tribologically induced nanocrystalline deformation microstructure at the contacting surface (a and b) and ~2 μm (c and d) and ~6 μm (e) below the contacting surface. Fig. 8 (a and b) reveal a nanocrystalline microstructure of largely equiaxed grains which, based on the almost continuous nature of the diffraction rings in the corresponding SADP insert (from the dashed red circled region), generally exhibit largely random orientations and high angle boundaries. However, the presence of some higher intensity elongated diffractions spots is also indicative of smaller regions and/or clusters of crystallites with small misorientations. In accord with XRD Fig. 3, this SADP confirms that the near surface matrix is principally austenite with a very small component of $\alpha/\alpha\prime$. Fig. 8(b) shows some intra-grain contrast variation due to dense dislocation structures, planar deformation structures and

Moire fringes. The crystallite boundaries are generally ill-defined and can appear wavy and diffused which is typical of severely deformed structures nanostructures due to, (i) the presence of non-equilibrium boundaries and excess extrinsic dislocations, (ii) internal substructures, and (iii), overlapping crystallites. These micrographs show no evidence of plastically extruded slithers at the contacting surface, therefore these microsgraphs are interpreted as coming from layer 2/3. However this is to be expected given the stochastic nature of wear.

At 2 μm below the contacting surface (Fig. 8(c and d)), the nanocrystalline microstructure is less developed, and shows larger, higher aspect ratio (elongated) nanograins relative to those observed in Fig. 8(a and b). Fig. 8(c) shows two carbide precipitates (indicated by white arrows) and their interaction with the matrix. More specifically, the elongated nanocrystalites are typically aligned or inclined towards the direction of matrix displacement (often the sliding/applied shear direction) which appears to be manipulated by the presence of carbides — giving the appearance that the plastic deformation of the matrix circumvents the carbide precipitates. Generally, the deformation structures/features are similar to those observed in Fig. 8(a and b), however the principal difference is that there appears to be a greater fraction of coherent boundaries and resolvable lath/planar like deformation structures.

At a depth of 6 μm beneath the contacting surface (Fig. 8(e) layer 2), the nanocrystalline deformation microstructure can be described as an evolving/gradient microstructure — the bounds of which can be defined by two clearly different deformation features, namely; (i) relatively large elongated high aspect ratio crystallites which often exhibit sharp high angle boundaries along their length (orange circle); and (ii),
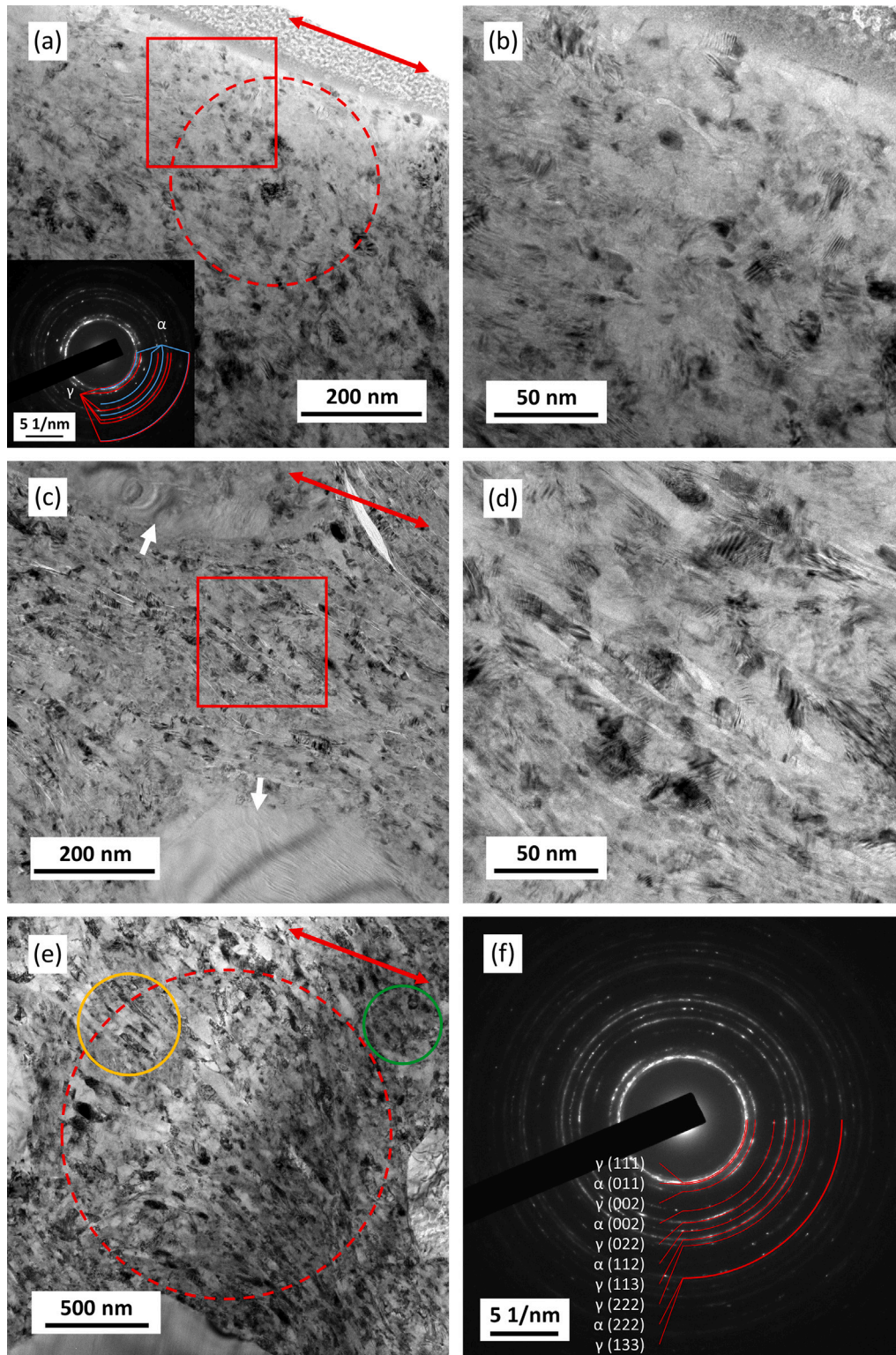
Fig. 8. (a–e) show BF-TEM micrographs depicting the tribologically induced nanocrystalline deformation microstructure at the contacting surface (a and b) as well as ~2 μm (c and d) and ~6 μm (e) below the contacting surface. The sliding direction is indicated by the red arrows in (a), (c) and (e). The higher magnification BF-TEM micrographs (b) and (d) correspond to the red boxed regions in (a) and (c) respectively. The SADP's (f) and the insert in (a) are from the areas marked with the dashed red circles in (e) and (a) respectively, and index to γ-Fe as the principal phase along with a small fraction of α/α′-Fe. The orange circle in (e) shows high aspect ratio crystallites, and the green circle in (e) shows crystallites with a reduced aspect ratio and ill-defined diffuse boundaries. (For interpretation of the references to colour in this figure legend, the reader is referred to the web version of this article.)

smaller more equiaxed nanocrystals with ill-defined diffuse boundaries (green circle). The co-existence of these deformation features shows that the latter almost certainly evolved into the former during deformation induced nanocrystalisation. The intra-crystallite contrast variation is interpreted as coming from dense dislocation arrangements(often planar in nature) and lath/planar deformation features (stacking faults and secondary twinning). Whilst these deformation structures often appear concurrently, there are a number of crystallites and/or regions within crystallites that appear to poses comparably low internal defect densities.

The elongated nanocrystals (orange circle), which are typically aligned or inclined towards the shear direction, are larger and exhibit the highest aspect ratio of all the BF-TEM microsgraphs presented in Fig. 8. Moreover, numerous elongated crystallites exhibit a large internal contrast variation which indicates that the misorientation and defect density along their length is high. Lower aspect ratio crystallites are, in some cases, seen to evolve from elongated crystallites because they can be assembled into the morphology of their parent elongated crystallite. The smaller more equiaxed nanocrystals (green circle) are analogous to those observed in Fig. 8(a–d), and their ill-defined boundaries, which are wavy and diffuse in character, are indicative of high-energy non-equilibrium boundaries and a excess of extrinsic dislocations.

Fig. 8(f) is a polycrystalline SADP from the dashed red circle in Fig. 8(e), and shows near continuous rings along with high intensity elongated diffraction spots for γ-Fe, as well a small fraction of $\alpha/\alpha\prime$-Fe which is seen as broken rings. This confirms the previous microstructural observations, more specifically: the continuous nature of the γ-Fe rings shows that the crystallites are largely randomly orientated with high angle boundaries; and the elongated γ-Fe diffraction spots indicate the presence of clusters of crystallites and/or localised regions with small misorientations. To summarise, the key microstructural observations from Fig. 8 are: (i) the nanocrystalline microstructre becomes increasingly more equiaxed closer to the contacting surface; (ii) the density of deformation induced planar defects is reduced and the coherent boundaries observed deeper below the surface are often transformed into high-angle boundaries; and (iii), the fraction of non-equilibrium boundaries increases closer to the contacting surface.

Fig. 9(a–b) confirms the presence of a sliding induced texture in the TAM when analysing a large number of crystallites over a large area directly adjacent to the contacting surface. Fig. 9(a) shows a BF-TEM micrograph of the nanocrystalline deformation structure (layer 2/3) and (b) shows a SADP from the red circled area in (a) which indexes to γ-Fe along with a small fraction of $\alpha/\alpha\prime$-Fe. The texture revealed by arching along the {111} and {220} diffraction rings; however, there exists a considerable spread and many orientations which do not conform to this texture. As such, this texture is best described as a diffuse S_1 (copper) type {111}⟨110⟩ shear texture aligned closely with the sliding (shear) direction. No evidence of the {100}⟨110⟩ or {110}⟨112⟩ could be found, however texture analysis is difficult due to the undulating nature of the tribologically affected surface. Similarly, the brass {112}⟨110⟩ shear texture was not observed, although the {224} diffraction ring is weak and this low SFE shear texture could not conclusively be ruled out.

Fig. 9(c) shows a BF-TEM micrograph of the nanocrystalline deformation structure ~5 μm beneath the contacting surface (layer 3). The SADP insert in (d) corresponds to the red circled region in (c) and indexes to both γ-Fe and $\alpha/\alpha\prime$-Fe. (d) is a DF-TEM micrograph from the same region in (c), taken using the $\alpha/\alpha\prime$-Fe diffraction ring (insert in (d)), and depicts a small number of deformed $\alpha/\alpha\prime$ crystallites. This shows that under these specific sliding conditions the SIM transformation to $\alpha\prime$-martensite, illustrated in Fig. 12, must be terminated earlier during deformation evolution in favour of other deformation modes, for example: twinning, dislocation slip, and grain boundary mediated deformation. Likewise, this SADP is in agreement with XRD (Fig. 3) and there is no evidence of ϵ-martensite in this near surface region.

3.6. Microstructural features of Layer 1

Fig. 10 shows BF-STEM micrographs (all taken with the same sample tilt) revealing the microstructural detail of the TAM at a distance of 60 μm beneath the contacting surface. Here the deformation microstructure is composed of lath-like structures, dark contrast needle structures forming at lath intersections, planar dislocation arrangements, stacking faults, dislocation lines and dislocation tangles. The intersections of planar deformation structures form a 70.5° angle with one another which is the angle between two {111} crystallographic planes (Fig. 10). Clearly, the secondary hard carbide phases (particles of different contrast to the deformed matrix) play a role in the accumulation and generation of defect structures as high densities of defects are generally observed surrounding them. At this location, lath and planar-type features appear dominant. The sliding direction is marked by the red arrows and a high density of planar defects is often observed parallel to this direction.

Fig. 10(c) shows the development of a very small dark contrast lath-like feature, indicated by a arrow, which appears to grow in the plane of an existing planar defect structure. This dark contrast lath has seemingly grown by the coalescence of individual segments of dark contrast within a region of high defect density. Additionally, these embryos appear to form at defect intersections which are finely spaced adjacent to one another. This observed growth mechanism may also explain the more developed dark contrast lath like structures observed in Fig. 10 which seemingly propagate from regions of high defect density namely lath intersections.

Fig. 11(a), from the same region as Fig. 10, shows a BF-TEM micrograph of a region rich in ϵ-martensite laths aligned parallel to the direction of sliding. Fig. 11(b) and (c) show the same SADP taken from the circled region in Fig. 11(a), and can be indexed to γ-austenite and ϵ-martensite. This SADP exhibits streaking which is consistent with stacking faults on the γ-Fe {111} planes. The ϵ-martensite diffraction spots reside as elongated regions of high intensity within these diffraction streaks, and this confirms that the ϵ-martensite is heavily flawed. Fig. 11(d) is a DF-TEM micrograph taken with the ϵ-martensite diffraction spot marked with the blue circle in Fig. 11(b). This confirms that a large fraction of the lath like structures are ϵ-martensite. Fig. 11(c) shows that the ϵ-martensite laths exhibit the Shorji-Nishiyama orientation relationship defined by $\{111\}_\gamma \parallel \{0001\}_\epsilon, \langle 10\bar{1}\rangle_\gamma \parallel \langle 11\bar{2}0\rangle_\epsilon$ with the parent γ-Fe phase.

Fig. 12(a) is a BF-TEM micrograph of several intersecting laths of ϵ-martensite and two dark contrast needle-like structures of $\alpha\prime$-martensite which form at the ϵ-martensite lath intersections. A large fraction of the ϵ-martensite is aligned parallel to the sliding direction which is indicated by the red arrow. Fig. 12(b) and (c) show the same SADP taken from the circled region in Fig. 12(a), and can be indexed to γ-austenite, ϵ-martensite (heavily flawed) and $\alpha\prime$-martensite, whilst streaking consistent with stacking faults on the γ-Fe {111} planes is also observed. The DF-TEM images, Fig. 12(d) and (e), have been taken with the ϵ-martensite diffraction spots denoted (d) (orange circle) and (e) (blue circle) in Fig. 12(b) respectively and confirm that the intersecting laths are ϵ-martensite. The DF-TEM micrograph, Fig. 12(f), has been taken with the isolated $\alpha\prime$-martensite diffraction spot marked as (f) (green circle) in Fig. 12(b), and shows that the needle like deformation structures which form at ϵ-martensite intersections are $\alpha\prime$-martensite. Fig. 12(c) shows that the $\alpha\prime$-martensite phase exhibits the Nishiyama-Wasserman orientation relationship $\{111\}_\gamma \parallel \{110\}_{\alpha\prime}, \langle 112\rangle_\gamma \parallel \langle 110\rangle_{\alpha\prime}$ with the γ phase.

To summaries, prior to nancrystalisation the deformation microstructure exhibits characteristics of low SFE materials and exhibits lath like structures, martensitic transformation and dislocation structures which are often planar in nature (layer 1). With increasing strain, closer to the contacting surface, the deformation microstructure becomes nanocrystalline and shifts from high aspect ratio crystalites to smaller more equiaxed crystallites with ill-defined non-equilibrium boundaries
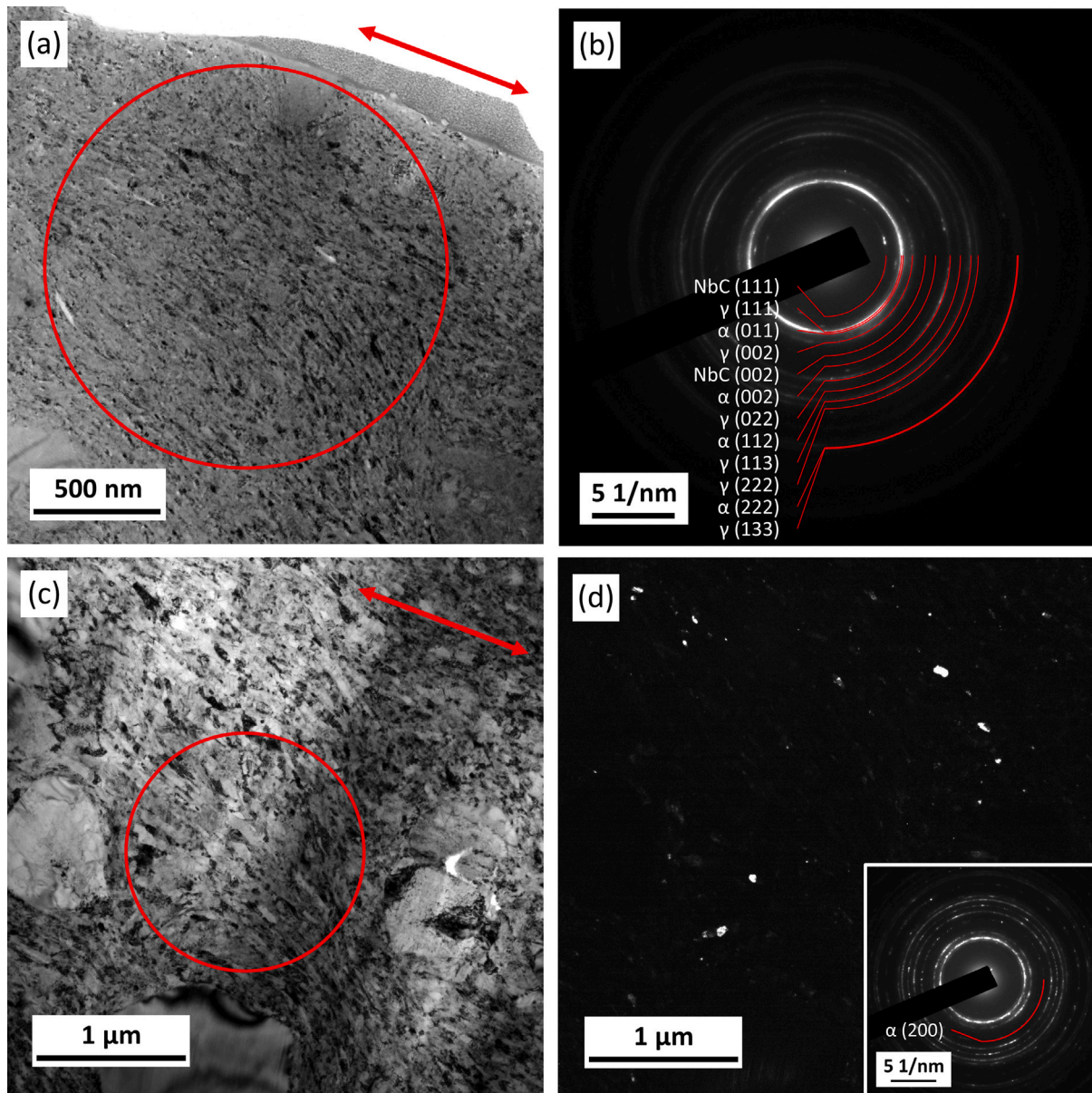
Fig. 9. (a) and (b) are BF-TEM micrographs depicting the microstructural detail of the tribologically induced nanostructure at the contacting surface and from ∼5 μm beneath the contacting surface. The sliding direction is indicated by the red arrows. The SADP's (b) and the insert in (d) are from the areas circled in red in (a) and (c) respectively. These confirm that γ-Fe as the principal phase along with a small fraction of $\alpha/\alpha\prime$-Fe. (d) is a DF-TEM micrograph of the same region show in (c), taken using the $\alpha/\alpha\prime$-Fe diffraction ring (insert in (d)).

(layer 2). Enormous strains are readily accommodated within this nanocrystalline layer, and this permits the formation of extruded slithers/striations of material at the contacting surface which subsequently allows the formation of ductile shear cracks (layer 3).

4. Discussion

During uniaxial tensile testing, the tensile strain to failure for HIPed Tristelle 5183 is reportedly <2% [18]. However, from inspection of the contacting surface (Fig. 2), it is clear that the subsurface shear strains generated during sliding are much greater than this tensile failure strain. The accommodation of such large plastic strains within the TAM can be explained by the plastic ratcheting phenomenon [1,47] in which large unidirectional plastic strains are incrementally accumulated during cyclic loading. The ratcheting phenomenon occurs when the so-called 'plastic shakedown limit' or the 'ratcheting threshold' is exceeded [1,47]; this can otherwise be described as the point when the

intensity of loading surpasses the yield criterion of the material even in the presence of protective residual stresses and strain hardening. This seemingly ductile response from Tristelle 5183 during sliding induced plastic ratcheting is a consequence of the high hydrostatic component of stress imposed by the sliding contact [2,47,48].

4.1. Layer 1 — Primary deformation modes

layer 1 (Figs. 10 to 12) (specifically at a distance of 60 μm from the contacting surface) exhibits many deformation structures including, ϵ-martensite laths, $\alpha\prime$-martensite, twins, planar defect intersections and planar dislocation arrangements (generated by planar slip) as well as stacking faults, dislocation lines and dislocation tangles. However, it would appear that the SFE of the γ-phase is sufficiently low that planar defects, for example martensite laths and planar dislocation arrangements, are the most frequently observed deformation features within this region of layer 1 (Figs. 10 to 12). All deformed grains exhibit
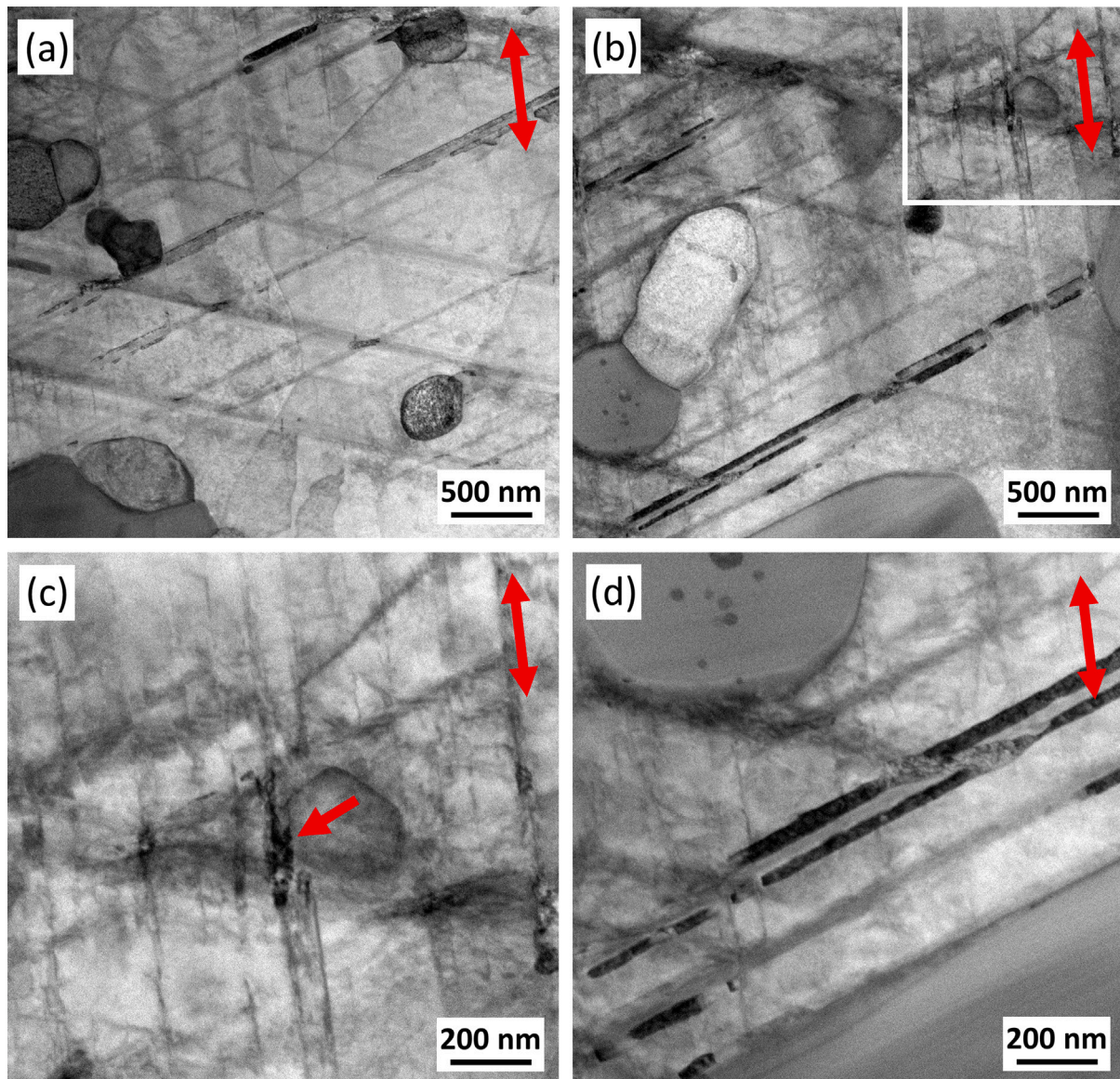
Fig. 10. Representative BF-STEM micrographs depicting the tribologically induced deformation structures in a FIB lamellae taken from 60 µm beneath the contacting surface (parallel to the sliding direction) following sliding contact testing. (c) shows the microstructural detail of the region marked with the white box in (b). The sliding direction is indicated by the red arrows. The particles of differing contrast to the deformed matrix are the secondary hard phase precipitates.

two or more activated slip systems, multiple variants of planar defect structures and extensive interactions between the volumetric planar defects (Fig. 10). In accord with the above, similar deformation structures have also been observed during the ambient temperature deformation of stainless-steel alloys with compositions that are analogous to the matrix composition of Tristelle 5183 [49–57].

The deformation structures within the γ-Fe phase are principally associated with the {111} planes, and their the intersection subdivides the matrix into sub-micron and nanoscale rhombic, trigonal and quadrilateral blocks (Fig. 10). In light of the above, it is postulated that the matrix microstructural refinement in layer 1 at a distance 60 µm from the contacting surface (Figs. 10 to 12) principally involves: (i) the formation of volumetric planar defects/deformation bands namely ϵ-martensite laths, twins and planar dislocation arrangements; and (ii), the intersection of multidirectional planar defects leading to grain subdivision and $\alpha\prime$-martensitic transformation. The shear direction (or direction of sliding) is parallel with one of the directions about which the planar volumetric defect boundaries form (Figs. 10 to 12). This

suggests that one of the fcc slip systems was possibly rotated towards, and subsequently activated along the direction of shear. The highest density of volumetric defects is generally observed in this direction which often generates elongated blocks aligned with the direction of shear (Figs. 10 to 12).

Secondary hard precipitates play a significant role in the generation and accumulation of defects within the matrix (Fig. 10), and defect rich deformation zones are induced around the precipitates. The mismatch in the mechanical properties between the matrix and secondary hard phase precipitates [35,58–62] means that complex multiaxial stress states are generated in the matrix and a stress gradient originating from the interphase interface during sliding is produced. This will assist with the activation of both faulting on all available {111} planes and slip systems and promote further work hardening. It is also suggested that some dislocation cross slip may be activated in these highly deformed regions which permits the increased formation of dislocation tangles and possibly even incipient dislocation walls (Fig. 10(c)). Within this deformation zone, the rate of dislocation and defect accumulation
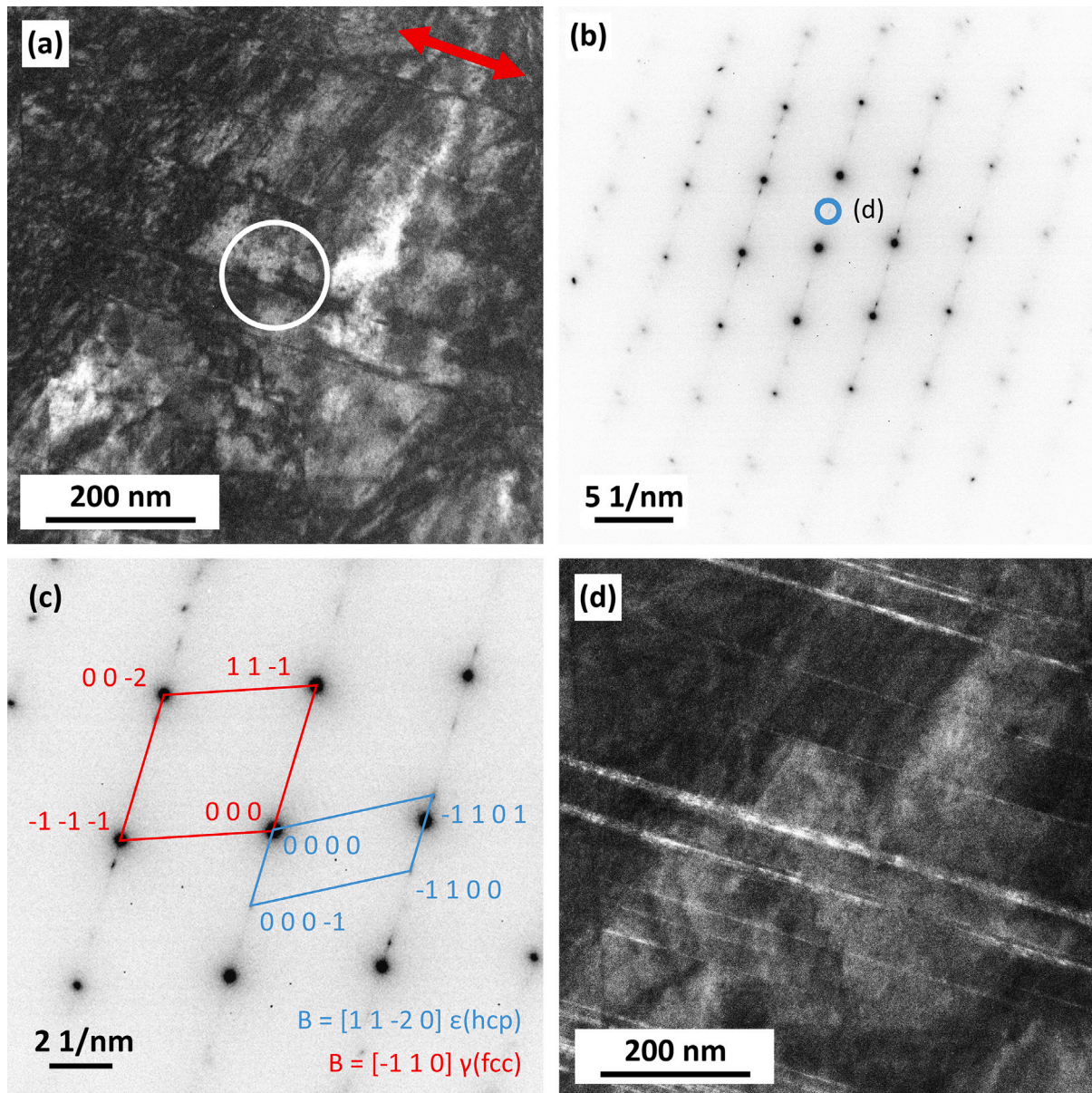
Fig. 11. TEM analysis illustrating the $\gamma \to \epsilon$ deformation induced martensitic transformation in Tristelle 5183. (a) shows a representative BF-TEM micrograph taken from 60 μm beneath the contacting surface (parallel to the sliding direction). (b and c) show the same select area diffraction pattern taken from the region marked with the white circle in (a). (c) shows that this SADP indexes to both fcc γ-Fe (red) and hcp ϵ-Fe (blue). (d) shows a DF-TEM micrograph of the same region depicted in (a), taken with the ϵ-Fe diffraction spot marked with the blue circle in (b). (For interpretation of the references to colour in this figure legend, the reader is referred to the web version of this article.)

increases which promotes rapid microstructural refinement [63,64] (Fig. 10).

Figs. 11 and 12 have shown that the γ (fcc) $\to \epsilon$ (hcp) (Fig. 11) and γ (fcc) $\to \epsilon$ (hcp) $\to \alpha\prime$ (bct) (Fig. 12) deformation induced martensite (DIM) transformation pathways dominate the formation of the ϵ (hcp) and $\alpha\prime$ (bct) phases during testing at 20 °C (60 μm below the contacting surface). However, martensite phases may also nucleate and form via different pathways at sites of crystallographic variability/discontinuity where the interaction energy favours martensitic transformation; for example, overlapping stacking faults, planar defect intersections (twin/transformation intersections), isolated planar defects, grain boundary — planar defect intersections and dislocation interactions et cetera [13,15,53,65–71]. The nature and occurrence of the deformation induced martensitic transformations in austenitic stainless steel is also susceptible to both the type of loading and strain rate [51,72,73]. In light of the above, the dominant DIM transformation mechanisms shown in Figs. 10 to 12 are most probably a result of the

specific matrix composition, the loading conditions imposed (60 μm below the contacting surface), and the temperatures induced during sliding.

The presence of elongated ϵ-martensite diffraction spots within the streaking due to staking faults on the γ-Fe {111} slip planes (Figs. 11 and 12) shows that the ϵ-martensite laths formed via the bundling of stacking faults; more specifically, the preferential formation of stacking faults adjacent to existing stacking faults typically on every second {111} slip plane. This bundling of stacking faults generates plate-like volumetric defects with the crystallography of heavily flawed hcp ϵ-martensite which exhibit the Shorji-Nishiyama orientation relationship with the parent γ-phase. This is in line with several other studies [13, 68,69] which suggest that the $\gamma \to \epsilon$ transformation occurs via an irregular overlapping process. More specifically, stacking faults form irregularly at first on the {111}$_\gamma$ slip planes after which further stacking faults are preferentially induced on nearby {111}$_\gamma$ planes as this is more
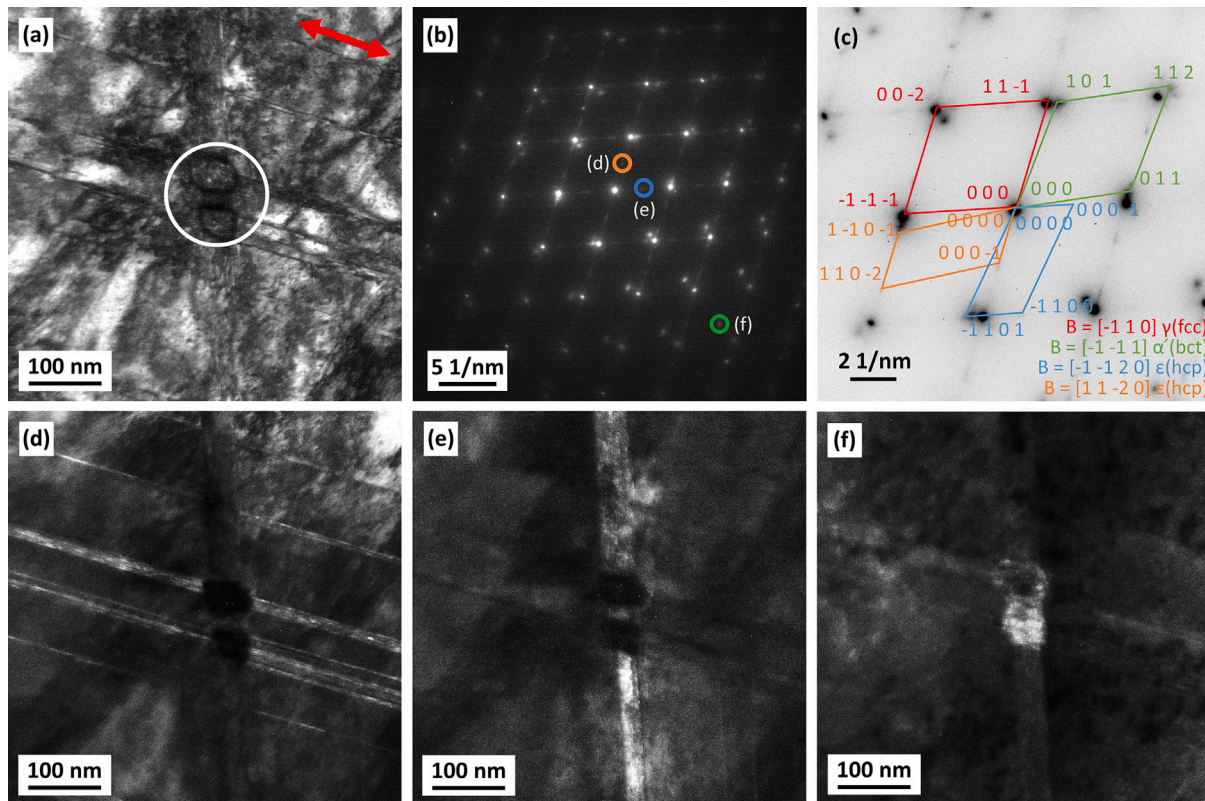
Fig. 12. TEM analysis illustrating the $\gamma \rightarrow \epsilon \rightarrow \alpha\prime$ deformation induced martensitic transformation in Tristelle 5183. (a) shows a representative BF-TEM micrograph taken from 60 μm beneath the contacting surface (parallel to the sliding direction). (b and c) show the same select area diffraction pattern taken from the region marked with the white circle in (a). (c) shows that this SADP indexes to fcc γ-Fe (red), bct $\alpha\prime$-Fe (green) and hcp ϵ-Fe (blue and orange). (d), (e) and (f) show DF-TEM micrographs of the same region depicted in (a). (d) was taken with the ϵ-Fe diffraction spot marked with the orange circle in (b). (e) was taken with ϵ-Fe diffraction spot marked with the blue circle in (b). (f) was taken with $\alpha\prime$-Fe diffraction spot marked with the green circle in (b). The sliding direction is indicated the by red arrow. (For interpretation of the references to colour in this figure legend, the reader is referred to the web version of this article.)

energetically favourable with regards to the minimisation of the bulk free energy and the total energy of the stacking faults.

$\alpha\prime$-martensite has been shown principally nucleate at the intersection between two ϵ-martensite laths and in this instance exhibits the Nishiyama-Wasserman orientation relationship with the γ-phase (Fig. 12(c)). The irregular contrast variation observed at these intersections (Fig. 12(d)) demonstrates that the $\alpha\prime$-martensite exhibits spatial inhomogeneities and can be regarded as irregular $\alpha\prime$-martensite embryos [74]. This is possibly the result of an irregular compliance of the necessary fault-displacements required for $\alpha\prime$-martensite transformation within the lath intersection. Fig. 10 shows that the dark contrast features (presumably $\alpha\prime$-martensite), which initially form at ϵ-martensite lath intersections, seemingly propagate out along the length of the lath in the form of separate closely stacked segments of $\alpha\prime$-martensite embryos. It is therefore postulated that the growth of the $\alpha\prime$-martensite phase occurs via the coalescence of closely spaced embryos of $\alpha\prime$-martensite at defect intersections along an ϵ-martensite lath. This nucleation and irregular grown mechanism is entirely consistent with previous observations on the growth of $\alpha\prime$-martensite in austenitic stainless steel [51,72,74].

4.2. Layer 1 — change of deformation mechanisms with depth

The deformation mechanisms observed ~60 μm beneath the contacting surface are expected to change/evolve as the depth beneath the contacting surface decrease. During the cyclic loading imposed during sliding, it is hypothesised that at a given distance below the contacting surface a critical threshold peak stress is reached which corresponds to a critical cross slip activity promoted by a specific long range internal stress state [75–77]. In terms of deformation evolution as the sample

surface is approached, it is suggested that an increased fraction of planar defects generates the specific long range internal stress state required for cross slip [75–77]. The specific long range internal stress state generated through the rapid accumulation of dislocations reduces the width of stacking faults and permits the cross slip of dislocations whilst reducing the interaction of partial dislocations that is otherwise required for transformation and twinning [78]. This shift in deformation mechanisms will also be influenced by the thermal gradients and possible adiabatic heating effects generated during sliding. This critical state of cross slip activity increases slip irreversibility and subsequently favours progressive deformation during sliding. The above hypothesis is analogous to the microstructural evolution observed during the plastic ratcheting of austenitic stainless steels with compositions which are comparable to the matrix composition of Tristelle 5183 [75,76,79–83]. Microstructurally, it is suggested that the critical activation of cross slip permits the formation of heterogeneous dislocation structures whereby the dislocation configuration evolves from low density dislocation configurations (Fig. 10) such as dislocation lines, planar dislocation arrangements and very light dislocation tangles to higher density dislocation arrangements such as heavy dislocation tangles, walls, veins and subsequently dislocation cells (dislocation trapping by polarised dislocation patterns) as the sample surface is approached. The increased activation of cross slip and the increased fraction of heterogeneous dislocation structures provides an explanation for the microstructures observed at ~25 μm below the contacting surface which is arguably more cellular in nature (Fig. 5(b)). This evolution in dislocation structures results in a further increase of work hardening as the sample surface is approached (Fig. 4).

To summarise, it is suggested that various modes of plastic deformation operate synergistically within layer 1 and the microstructure

evolves as the sample surface is approached such that the fine networks of volumetric planar defects, intersecting planar defects, dislocation interactions, heterogeneous dislocation structures and dislocation cells comprehensively restrain the microstructure from further plastic deformation via the dislocation mediated modes of deformation. This microstructural evolution permits the incremental accommodation of large strains during the cyclic loading imposed by sliding. However, the generation, accumulation and interaction of these defect structures is known to be a precursor to shear localisation [8,84–86].

4.3. Evaluating the tribologically affected material via XRD

XRD from the tribologically affected surface (Fig. 3) shows that only a small fraction of the γ-Fe matrix undergoes the deformation induced martensitic transformation to $\alpha\prime$-martensite. Nevertheless, this transformation appears to be saturated (under these specific sliding conditions), and no evidence of the intermediary ϵ-martensite phase is observed within the uppermost regions of the TAM contributing to the diffracted signal in XRD. However, the ϵ-martensite phase is observed via TEM 60 μm beneath the contacting surface (Figs. 10 to 12) and, at this depth, the γ (fcc) → ϵ (hcp) → $\alpha\prime$ (bct) transformation pathway has been identified as the principle mode through which $\alpha\prime$-martensite is generated during sliding. The ϵ-martensite observed 60 μm beneath the contacting surface must therefore further evolve and transform as the contacting surface is approached in order to remain consistent with the absence of ϵ-martensite in XRD (Fig. 3). It is possible that as the surface is approached, further transformation to ϵ-martensite is suppressed and $\alpha\prime$-martensite may be generated via alternative pathways which may consume the remaining ϵ-martensite. Regardless, under these sliding conditions the total fraction of $\alpha\prime$-martensite is seemingly restricted even though the TAM contributing to the diffracted signal in XRD (~8 μm beneath the contacting surface) has been exposed to extensively high strains (Figs. 2, 4, 5, 7 and 8) at testing temperatures below the M_d temperature of Tristelle 5183. Other deformation modes are seemingly more energetically favourable as the sample surface is approached and DIM is seemingly terminated and saturated in a premature state under these specific sliding conditions.

4.4. Layer 2 — nanocrystallisation and strain localisation

TEM of the near surface has shown a deformation microstructure which evolves from ultrafine/nanoscale high aspect ratio (elongated) crystallites generally aligned parallel to the direction of shear with high angle boundaries, to a more equiaxed nanocrystalline microstructure of grains which typically exhibit largely random orientations and high angle boundaries (Figs. 7 to 9). It is therefore suggested that as the surface is approached, the dislocation mediated modes of deformation observed in layer 1 become less dominant, the subsurface becomes unstable, and a nanocrystalline microstructure is generated within layer 2 as a result in a shift in the modes of deformation. These nanocryataline microstructures are analogous to those observed during shear localisation and are consistent with the accommodation of large strains principally by grain boundary mediated deformation mechanisms (e.g. grain boundary sliding/migration, grain rotation and grain boundary diffusion) and crystallographic slip [8,84–86]. The ability to sustain high levels of deformation within layer 2 is clearly a result of the specific loading conditions of simple shear (torsion) and compression where a high hydrostatic component of stress is generated. Furthermore, the deformation mechanisms and microstructural evolution within layer 2 may be influenced by adiabatic heating during the localisation phenomena and the flash temperatures and thermal gradients induced by sliding.

It is suggested that high accumulations of defects, for example transformation/twin networks and dislocation structures including heterogeneous dislocation cells, provide the pre-requisite for a sudden release of deformation energy that is the driving force for observed nanocrystalline microstructure. This hypothesis is analogous to the microstructural evolution reported during shear localisation [84–86]. As such, it is postulated that tribolocially induced nanocrystallisation occurs when dislocation mediated modes of deformation can no longer readily accommodate the strains imposed upon the material. Deformation mechanisms (for example transformation and twinning) are restricted and grain boundary mediated deformation mechanisms and crystallographic slip during nanocrystallisation are the principal modes of plastic deformation. Prior to and/or during the initial stages of nanocrystallisation, elongated microstructural features are generated in the direction of shear probably by: (i) heterogeneous dislocation structures (specifically dislocation cells) which become elongated due to plastic deformation, or (ii), lath like microstructures generated via primary/secondary deformation twinning. With specific reference to dislocation cells, the lateral dislocation walls which are aligned parallel with the direction of shear are thinned due to dislocation annihilation and new boundaries may be formed [86].

TEM observations have shown that that dislocation activity must still play a role in nanocrystallisation. It is further hypothesised that the evolution and refinement of the nanocrystalline microstructure observed in layer 2 (Figs. 7 and 8) is, in part, influenced by an avalanche of dislocations which assists with the near surface localised flow of material. This is based on the observation that layer 2 contains elongated crystallites which exhibit large internal misorientations generally along their length (Fig. 8). These large misorientations are most probably the product of domains of high and low defect (dislocation) density resulting in large contrast variations within a given elongated crystallite (Fig. 8). During sliding, dislocation accumulations, such as dislocation tangles or pile ups may form along the length (often at the ends) of elongated crystallites. Dislocations continue to accumulate within these elongated crystallites and separate domains that are composed of high and low dislocation/defect densities are formed. These domains of dense dislocations become thicker and thicker until the elongated microstructural features collapse, breakdown or split and new boundaries are formed [8,86]. This process, which is often termed the avalanche of dislocations, is dominated by (internal) crystallographic slip and observed throughout the entirety of the nanocrystalline deformation layer (Figs. 7 and 8). This confirms that crystallographic slip and the avalanche of dislocations is an important deformation mode which assists with strain accommodation within layer 2 of the TAM. This breakdown of elongated crystallites appears to heavily influence the microstructural evolution/refinement within layer 2.

It is postulated that strain accommodation within the nancrystalline region is also heavily influenced by grain boundary mediated deformation mechanisms which differ from the purely dislocation mediated deformation modes observed in layer 1 (and other course grained materials). Once a nanocrystalline structure is generated in layer 2 (Figs. 7 and 8), large strains are believed to be principally accommodated by grain boundary mediated deformation modes including grain boundary sliding and rotation. This hypothesis is proposed based on two observations: (i) the width of elongated crystallites is subject to very slow/little microstructural refinement during shear deformation (as the contacting surface is approached); and (ii), the most notable microstructural variation/evolution occurs via the breakdown of elongated crystallites which is reliant on internal dislocation slip (Figs. 7 and 8). If the large strains accommodated within layer 2 are completely accounted for by internal dislocation slip, one would expect both a potent breakdown and narrowing in the width of the elongated crystallites within layer 2. However, this is not the case and indicates that grain boundary mediated deformation mechanisms are important in the accommodation of the enormous strains observed within layer 2.

Within the nanocrystalline layer, globular nanoscale regions are seemingly generated which possess both a roughly uniform crystalline orientation and defect density, and thus appear to have similar contrast in Fig. 8. The dimensions of these regions are seemingly larger than the parent microstructural features (elongated crystallites), and appear

to be composed of multiple different crystallites. This observation further strengthens the theory that grain boundary mediated deformation mechanisms (namely grain boundary slip and rotation) are an essential mode of strain accommodation within the nanocrystalline layer. This hypothesis is consistent with both the microstructures and deformation mechanisms previously reported during severe plastic deformation involving nanocrystalline principally austenitic microstructures [49,64, 84–86]. Grain boundary mediated deformation within shear banded microstructures has also been reported [84], and it is believed to play a significant role in the accommodation of shear through both the rotation of individual crystallites and clusters of crystallites.

Notable strains may still be accommodated via crystallographic slip within layer 2 because the small dislocation path length associated with the ultrafine/nanocrystalline microstructure means that dislocations can be readily and easily incorporated within the high angle crystallite boundaries (Fig. 8). Additionally, the probability of dislocation interaction events within a given crystallite is reasonably low due to the small dislocation path length. Therefore, the development of the internal dislocation accumulations (and low angle boundaries) that are required for microstructural evolution and refinement requires large strains [8] (Figs. 7 and 8). It is also suggested that dynamic recovery in the initial stages of nanocrystallisation may aid with the formation of low-angle boundaries. It is postulated that a large fraction of dislocations are simply consumed within the crystallite boundaries which means that the rate of microstructural evolution and strain hardening is low relative to the strains which are accommodated via crystallographic slip within layer 2 (Figs. 7 and 8). However, this mode of deformation may be important as grain boundary sliding, grain rotations, and dislocation slip deformation modes have been reported to strongly influence one another [87–89].

Other mechanisms may also be important in the evolution of the microstructure generated within layer 2, particularly during the early stages of nanocrystallisation. By way of example, given that γ-Fe (fcc) has 24 available twin systems operative on the {111} planes, a deformation induced rotation inside or outside the nanocrystalline layer may easily permit the activation of twin systems which become orientated towards the direction of shear. In this instance, twins will rapidly multiply and a state of saturation with be reached which generates a microstructure of fine laths [86]. This microstructure will subsequently further evolve in line with the other mechanisms outlined above. More generally, deformation induced rotations may permit the activation of deformation twin and slip systems (also on the {111} plane) which will readily generate elongated microstructures aligned with the direction of shear. Sliding induced rotations which permit the preferred alignment of the {111} planes parallel to the sliding direction may be a factor that contributes to the preferred alignment of the {111} planes parallel to the siding direction observed in the XRD patterns (Fig. 3). This preferred alignment is one factor which causes an increase in the relative peak height of the $\{111\}_\gamma$ reflection following testing compared to as received Tristelle 5183.

The microstructures within layer 2 (Figs. 7 and 8) retain a lineage with the original deformation microstructure prior to nanocrystallisation, whereby the breakdown of high aspect ratio (elongated) microstructural features suggests that they may have directly evolved from elongated lath type microstructures. Therefore, dynamic recovery followed by continuous dynamic recrystallisation (CDRX) resulting in microstructural refinement are believed to be the principal mechanisms controlling the microstructural development within the nanocrystalline regions beneath the contacting surface [84,86,90,91]. This microstructural evolution mechanism is supported by the diffuse deformation texture within the nanocrystalline region which conforms to the S1 type where the strongest component at the near surface is {111}⟨110⟩, typically tilted up to 10 ° from the sliding direction (Fig. 8). Discontinuous dynamic recrystallisation (DDRX) is believed not to be operative as there appears to be no nucleation/growth period and the nanocrystalline regions are not composed of defect-free equiaxed

grains which are typically observed in DDRX materials (Figs. 7 and 8) [90]. Likewise, within the nanocrystalline region, a large fraction of boundaries appear ill-defined which is a significant deviation from nucleation/growth type of recrystallised grains. No recrystallisation texture was observed (Fig. 8) which further supports the idea that the microstructure evolves via CDRX as opposed to DDRX. The high degree of random orientation does however support the argument that recrystallisation has taken place in the form of continuous dynamic recrystallisation.

TEM (Figs. 7 and 8) shows that carbides have a profound effect on the nanocrystallisation phenomena, whereby hard carbide phases clearly act as impenetrable barriers to localisation (shear banding) and disrupt the localised deformation pattern of elongated matrix crystallites in the immediate vicinity of the carbides. The mismatch in the mechanical properties between the carbide and matrix phases means complex multiaxial stresses are induced in the matrix during sliding; this distorts the localised direction of plastic flow (the direction of shear) which would otherwise be aligned parallel to the sliding direction. This explains the wavy appearance of the matrix crystallite deformation pattern within layer 2 (Figs. 7 and 8) which directly relates to the presence of carbides. Considering the above, it is hypothesised that the presence of carbides will increase the critical strains for nanocrystallisation and to some minor extent homogenise and distribute shear (Figs. 7 and 8).

4.5. Layer 3 — the tribological interaction layer

Layer 3 (Fig. 4) is highly variable and encompasses many tribological phenomena including (but not limited to) the plastic ratcheting of extruded slivers, fracture, mechanical mixing, tribochemical reactions and oxidation. However, layer 3 can more generally be defined as layer directly adjacent to the interface within which material removal (debris generation) and both physical and chemical interactions with the environment and counterface occur. The details of the interacting tribological phenomena which are observed at the contacting surfaces during sliding contact testing will be discussed in the following section.

Following testing, highly deformed striations/slivers of mechanically mixed material, which are principally metallic in nature, have been identified at the contacting surface (Figs. 2, 5 and 7). These tribological layers are characteristic of plasticity dominated wear [43, 92–97] which is almost certainly the principal mechanism governing the degradation of Tristelle 5183. A number of theories have been proposed in the literature which attempt to identify the mechanisms of degradation leading to the generation of plate/flake-like debris during plasticity dominated wear [1–6]. Nevertheless, two notable mechanisms of plasticity dominated wear have been identified in the literature which provide some insight into the generation of the thin plate type wear features and debris observed in the present study. Firstly, the extrusion of thin slivers via plastic ratcheting which subsequently break off [1,2,47]. Fracture does not play an intrinsic role in this wear mechanism and fracture is only relevant to the detachment of the extruded slivers. Secondly, crack nucleation and propagation via the fracture of a thin surface layer resulting in detachment (often termed 'delamination' wear) [6,98]. The latter of these two mechanisms can be related to surface failure via low cycle fatigue [99,100]. However, both of these wear mechanisms can be linked to the plastic ratcheting phenomenon. Therefore degradation can be more generally described as 'wear by plastic ratcheting' [47] as, irrespective of the failure mode, large subsurface strains have been accommodated via plastic ratcheting which provides the necessary criterion/condition for near surface failure. In light of the this, two competing failure modes have been identified [47,101], specially: (i) material detachment when the accumulated strain reaches a critical value (this is analogous to the strain to failure observed in monotonic tests and is termed ratchetting failure), and (ii), failure by low cycle fatigue.

In the present study, plastic ratcheting and extrusion leading to fracture seems to be the most dominant mode of plasticity dominated wear. The accumulation of strain via ratcheting generates a tribological layer within which the deformation structures are inherently more heterogeneous relative to the rest of the TAM and often composed of numerous discernible layers (Figs. 5 and 7). The thickness of this tribological layer is highly variable and typically of the order of 0–10 μm (Figs. 5 and 7). It is clear that a large fraction of the so-called subsurface cracks are in fact generated via extrusion; this is made evident by the observation of extruded plate-like features, gross plastic deformation, and the presence of cracking in heavily plastically deformed material (Figs. 2, 5, 7 and 8). It is postulated that these so-called subsurface cracks (Figs. 2, 5 and 7) grow each loading cycle and can be regarded as ductile shear cracks which are governed by plastic strain [2] and not by elastic stress intensity conventionally used in linear elastic fracture mechanics [102,103]. Based on these observations, it seems probable that ratcheting failure is the dominant mode of failure resulting in material detachment.

Whilst the plastic ratcheting phenomenon provides one with a dominant mechanism of material detachment, some additional consideration needs to be made concerning material transfer, mechanical mixing, and 'third body' effects within the tribological environment. Mechanical mixing permitted by the plastic ratcheting phenomenon also appears to be prevalent throughout the tribological layer and the evidence for this has been provided by three notable observations. Firstly, isolated fragments of both NbC and M_7C_3 exist in the tribological layer (Figs. 5 and 7) which can only have formed via fragmentation followed by mechanical mixing with the matrix. Secondly, the matrix composition in the tribological layer is inhomogeneous and deviates from that of the bulk following testing (Fig. 7). In this self-mated sliding situation, the chemical modification of the tribological layer is most probably a result of chemical interaction (possibly oxidation) and mechanical mixing within the wearing environment [93]. Finally, the extensive strains accommodated within the tribological layer can only have been achieved in conjunction with mechanical mixing where the principal deformation modes are grain boundary mediated as well as a contribution from crystallographic slip.

The transfer phenomenon is inherently difficult to investigate and confirm within self-mated sliding systems [93]. However, it seems unlikely that a detached plate-like feature is instantaneously ejected from between the contact without further interaction with the contacting surfaces. Therefore, it is hypothesised that an element of material may be transferred, reattached to either of the contacting surfaces, and further deformed prior to debris ejection from within the wear track. During steady state wear, it is suggested that the following transfer phenomena may occur: (i) the repeated transfer of previously transferred material, (ii) the integration and transfer of previously undetached material, or (iii), the formation of new transfer elements. During steady state sliding, the repeated adhesion, deformation, and transfer of material at the interface may lead to the generation of a plate-like wear particle [43,92]. This plate-like wear particle (third body) is either ejected from the contacting surfaces (Fig. 6) or re-integrated within the contacting surface. Regardless, based on the observations made in the present work, it seems probable that the generation of a tribological layer is necessary for material detachment during steady state wear.

The in-depth analysis of the deformation evolution within the TAM has shown that nanocrystalisation driven by concurrent operation of grain boundary mediated deformation mechanisms and crystallographic slip is fundamentally important in the accommodation of extensive strain during plastic ratchetting. Additionally, the loading conditions imposed during sliding (simple shear and compression) generate a high hydrostatic component of stress which permits the somewhat ductile response of an alloy that would otherwise be considered brittle. It is therefore postulated that nanocrystalisation principally driven by grain boundary mediated deformation and crystallographic slip within the TAM is intrinsically linked to the plasticity-dominated wear phenomenon which is crucial to the degradation of the sliding contact investigated in the present study. In other words, regardless of the mode of surface failure discussed above, nanocrystalisation is considered to be essential for plasticity-dominated wear to be operative. The TAM succumbs to nanocrystalisation and extensive grain boundary mediated deformation and crystallographic slip at depths up to approximately several tens of micron beneath the contacting surface. Therefore, under the present sliding conditions, Tristelle 5183 is incapable of suppressing the detachment of microscale debris via plasticity dominated wear.

The presence of tribological layers greatly influences the contact state of the frictional surfaces and acts to partially suppress the extent of subsurface deformation by accommodating large shear strains [43]. Under the contacting conditions employed in this work, the presence of a stable metallic tribological layer seemingly suppresses the onset of deep penetrating gross plastic deformation and transfer. Unfortunately, the tribological layer is clearly readily removed and subsequently replenished by either the underlying zones or the counterface once a steady state sliding wear regime is established.

5. Conclusions

1. The tribologically affected material (TAM) can be described as a continuum of deformation which results from a strain gradient where the highest strains are generated at the sliding interface.
2. The initial mechanisms of plastic deformation within the TAM (furthest from the sliding contact) are dislocation mediated and include: deformation induced martensitic transformation to ϵ-martensite and $\alpha\prime$-martensite principally via the $\gamma \rightarrow \epsilon$ and $\gamma \rightarrow \epsilon \rightarrow \alpha\prime$ transformation pathways, twinning, the generation of planar dislocation arrangements (generated by planar slip) and the generation of dislocation tangles.
3. Within the higher strained regions of the TAM (closer to the contacting surface), the initial (dislocation mediated) modes of plastic deformation become less dominant, the subsurface becomes unstable, and localised shear driven by grain boundary mediated deformation mechanisms and crystallographic slip completely engulf the near surface microstructure. A nanocrystalline microstructure is generated in the near surface and large strains are accommodated by the concurrent operation of these nanocrystalline deformation modes.
4. High levels of strain prior to failure are permitted due to the specific loading conditions of simple shear (torsion) and compression where a high hydrostatic component of stress is generated.
5. Tribological degradation is principally governed by plasticity dominated wear which is reliant on nanocrystalisation and the associated accumulation of extremely high strains within the subsurface. The extrusion of metallic slivers via plastic ratcheting generates ductile shear cracks governed by plastic strain, and the failure of these slivers generates plate/flake-like wear debris.

CRediT authorship contribution statement

M.J. Carrington: Conceptualization, Data curation, Formal analysis, Investigation, Methodology, Resources, Software, Validation, Visualization, Writing – original draft, Writing – review & editing. **J.L. Daure:** Project administration, Resources. **S. Utada:** Investigation. **V.L. Ratia-Hanby:** Investigation. **P.H. Shipway:** Conceptualization, Supervision, Writing – original draft, Writing – review & editing. **D.A. Stewart:** Funding acquisition, Supervision. **D.G. McCartney:** Conceptualization, Supervision, Validation, Writing – original draft, Writing – review & editing.

Declaration of competing interest

Data availability

Data will be made available on request.

Acknowledgements

References

[1] A. Kapoor, K. Johnson, Plastic ratchetting as a mechanism of metallic wear, Proc. R. Soc. London. Ser. A: Math. Phys. Sci. 445 (1924) (1994) 367–384.

[2] K. Johnson, Contact mechanics and the wear of metals, Wear 190 (2) (1995) 162–170.

[3] T. Kjer, A lamination wear mechanism based on plastic waves, Wear Mater. 1 (1987) 191–198.

[4] D. Rigney, The role of characterization in understanding debris generation, in: Tribology Series, vol. 21, Elsevier, 1992, pp. 405–412.

[5] E. Kopalinsky, P. Oxley, Explaining the mechanics of metallic sliding friction and wear in terms of slipline field models of asperity deformation, Wear 190 (2) (1995) 145–154.

[6] N. Suh, The delamination theory of wear, Wear 25 (1) (1973) 111–124.

[7] B. Yao, Z. Han, K. Lu, Correlation between wear resistance and subsurface recrystallization structure in copper, Wear 294 (2012) 438–445.

[8] W. Rainforth, R. Stevens, J. Nutting, Deformation induced by sliding contact, Phil. Mag. A 66 (4) (1992) 621–641.

[9] L. Remy, A. Pineau, Twinning and strain-induced F.C.C. → H.C.P. transformation in the Fe-Mn-Cr-c system, Mater. Sci. Eng. 28 (1) (1977) 99–107.

[10] D. Pierce, J. Jiménez, J. Bentley, D. Raabe, J. Wittig, The influence of stacking fault energy on the microstructural and strain-hardening evolution of Fe–Mn–Al–Si steels during tensile deformation, Acta Mater. 100 (2015) 178–190.

[11] S. Curtze, V. Kuokkala, Dependence of tensile deformation behavior of TWIP steels on stacking fault energy, temperature and strain rate, Acta Mater. 58 (15) (2010) 5129–5141.

[12] D. Pierce, J. Jiménez, J. Bentley, D. Raabe, C. Oskay, J. Wittig, The influence of manganese content on the stacking fault and austenite/ε-martensite interfacial energies in Fe–Mn–(Al–Si) steels investigated by experiment and theory, Acta Mater. 68 (2014) 238–253.

[13] D. Kaoumi, J. Liu, Deformation induced martensitic transformation in 304 austenitic stainless steel: In-situ vs. ex-situ transmission electron microscopy characterization, Mater. Sci. Eng. A 715 (2018) 73–82.

[14] J. Breedis, L. Kaufman, The formation of Hcp and Bcc phases in austenitic iron alloys, Metall. Trans. 2 (9) (1971) 2359–2371.

[15] P. Mangonon, G. Thomas, The martensite phases in 304 stainless steel, Metall. Trans. 1 (6) (1970) 1577–1586.

[16] J. Talonen, H. Hänninen, Formation of shear bands and strain-induced martensite during plastic deformation of metastable austenitic stainless steels, Acta Mater. 55 (18) (2007) 6108–6118.

[17] P. Crook, R. Zordan, Nuclear grade steels, 1987, US Patent 4, 643, 767.

[18] C. Zhao, D. Stewart, J. Jiang, F. Dunne, A comparative assessment of iron and cobalt-based hard-facing alloy deformation using HR-EBSD and HR-DIC, Acta Mater. 159 (2018) 173–186.

[19] News & Views, Powder Metall. 36 (2) (1993) 77–97.

[20] W. Burdett, Development of cobalt free wear resistant alloys for nuclear applications, Surf. Eng. 8 (2) (1992) 131–135.

[21] S. Shiels, W. Wilson, K. Rosengarth, G. Wire, Laboratory Evaluation of Low Cobalt Wear Materials for Nuclear Applications, Technical Report, Bettis Atomic Power Laboratory, 1994.

[22] B. Cockeram, Corrosion resistance and electrochemical potentiokinetic reactivation testing of some iron-based hardfacing alloys, Corrosion 56 (8) (2000) 849–859.

[23] E. Murphy, I. Inglis, Endurance Tests of Valves with Cobalt-Free Hardfacing Alloys: PWR Phase, Technical Report, Electric Power Research Inst., 1992.

[24] J. Siefert, D. Gandy, Program on Technology Innovation: Galling and Sliding Wear Test Results for Candidate Hardfacing Alloys Manufactured by Power Metallurgy and Hot Isostatic Pressing (PM/HIP), Technical Report, Electric Power Research Inst., 2013.

[25] J. Daure, M. Carrington, D. McCartney, D. Stewart, P. Shipway, Measurement of friction in galling testing–An example of its use in characterising the galling behaviour of hardfacings at ambient and elevated temperature, Wear (2021) 203736.

[26] R. Smith, J. Siefert, D. Gandy, S. Babu, Tribolayer formation by strain-induced transformations in hardfacing alloys, in: D. Gandy, J. Shingledecker (Eds.), Advances in Materials Technology for Fossil Power Plants, ASM International, Materials Park, OH, 2014, pp. 482–490.

[27] H. Ocken, Reducing the cobalt inventory in light water reactors, Nucl. Technol. 68 (1) (1985) 18–28.

[28] H. Ocken, The galling wear resistance of new iron-base hardfacing alloys: A comparison with established cobalt-and nickel-base alloys, Surf. Coat. Technol. 76 (1995) 456–461.

[29] J. Sulley, D. Stewart, HIPed hard facings for nuclear applications: Materials, key potential defects and mitigating quality control measures, in: 2016 24th International Conference on Nuclear Engineering, American Society of Mechanical Engineers, 2016.

[30] H. Atkinson, B. Rickinson, Hot Isostatic Processing, Springer, 1991.

[31] M. Carrington, J. Daure, V. Ratia, P. Shipway, D. McCartney, D. Stewart, Microstructural characterisation of Tristelle 5183 (Fe-21%Cr-10%Ni-7.5%Nb-5%Si-2%c in wt%) alloy powder produced by gas atomisation, Mater. Des. 164 (2019) 107548.

[32] V. Ratia, D. Zhang, M. Carrington, J. Daure, D. McCartney, P. Shipway, D. Stewart, The effect of temperature on sliding wear of self-mated HIPed Stellite 6 in a simulated PWR water environment, Wear 420 (2019) 215–225.

[33] V. Ratia, D. Zhang, M. Carrington, J. Daure, D. McCartney, P. Shipway, D. Stewart, Comparison of the sliding wear behaviour of self-mated HIPed Stellite 3 and Stellite 6 in a simulated PWR water environment, Wear 426 (2019) 1222–1232.

[34] M.J. Carrington, J. Daure, V.L. Ratia-Hanby, D. Zhang, P.H. Shipway, D.A. Stewart, D.G. McCartney, Microstructural characterisation of subsurface deformation and the degradation of stellite 6 induced by self-mated sliding contact in a simulated PWR environment, Tribol. Int. 158 (2021) 106899.

[35] D. Bowden, Y. Krysiak, L. Palatinus, D. Tsivoulas, S. Plana-Ruiz, E. Sarakinou, U. Kolb, D. Stewart, M. Preuss, A high-strength silicide phase in a stainless steel alloy designed for wear-resistant applications, Nat. Commun. 9 (1) (2018) 1–10.

[36] D. Bowden, D. Stewart, M. Preuss, Understanding the microstructural evolution of silicide-strengthened hardfacing steels, Mater. Des. 161 (2019) 1–13.

[37] D. Bowden, D. Stewart, M. Preuss, The identification of a silicide phase and its crystallographic orientation to ferrite within a complex stainless steel, J. Nucl. Mater. 517 (2019) 356–361.

[38] R. Young, The Rietveld Method, Vol. 6, Oxford university press Oxford, 1993.

[39] R. Cheary, A. Coelho, A fundamental parameters approach to X-ray line-profile fitting, J. Appl. Crystallogr. 25 (2) (1992) 109–121.

[40] R. Cheary, A. Coelho, J. Cline, Fundamental parameters line profile fitting in laboratory diffractometers, J. Res. Natl. Inst. Stand. Technol. 109 (1) (2004) 1.

[41] R.M. Langford, A.K. Petford-Long, Preparation of transmission electron microscopy cross-section specimens using focused ion beam milling, J. Vac. Sci. Technol. A 19 (5) (2001) 2186–2193.

[42] M.J. Carrington, D.G. McCartney, P.H. Shipway, D.A. Stewart, Microstructure formation in the powder hiped hardfacing alloy tristelle 5183 (Fe-21% Cr-10% Ni-7.5% Nb-5% Si-2% C in wt%), Mater. Charact. 184 (2022) 111688.

[43] I. Hutchings, P. Shipway, Tribology: Friction and Wear of Engineering Materials, Butterworth-Heinemann, 2017.

[44] B. Cullity, Elements of X-Ray Diffraction, Addison-Wesley Publishing, 1956.

[45] J. Dautzenberg, J. Zaat, Quantitative determination of deformation by sliding wear, Wear 23 (1) (1973) 9–19.

[46] W. Cai, P. Bellon, Microstructural self-organization triggered by twin boundaries during dry sliding wear, Acta Mater. 60 (19) (2012) 6673–6684.

[47] A. Kapoor, Wear by plastic ratchetting, Wear 212 (1) (1997) 119–130.

[48] M. Yajima, M. Ishii, M. Kobayashi, The effects of hydrostatic pressure on the ductility of metals and alloys, Int. J. Fract. Mech. 6 (2) (1970) 139–150.

[49] H. Zhang, Z. Hei, G. Liu, J. Lu, K. Lu, Formation of nanostructured surface layer on AISI 304 stainless steel by means of surface mechanical attrition treatment, Acta Mater. 51 (7) (2003) 1871–1881.

[50] M. Jayalakshmi, P. Huilgol, B. Bhat, K. Bhat, Insights into formation of gradient nanostructured (GNS) layer and deformation induced martensite in AISI 316 stainless steel subjected to severe shot peening, Surf. Coat. Technol. 344 (2018) 295–302.

[51] V. Shrinivas, S. Varma, L. Murr, Deformation-induced martensitic characteristics in 304 and 316 stainless steels during room-temperature rolling, Metall. Mater. Trans. A 26 (3) (1995) 661–671.

[52] J. Brooks, M. Loretto, R. Smallman, In situ observations of the formation of martensite in stainless steel, Acta Metall. 27 (12) (1979) 1829–1838.

[53] Y. Shen, X. Li, X. Sun, Y. Wang, L. Zuo, Twinning and martensite in a 304 austenitic stainless steel, Mater. Sci. Eng. A 552 (2012) 514–522.

[54] T. Byun, E. Lee, J. Hunn, Plastic deformation in 316LN stainless steel–characterization of deformation microstructures, J. Nucl. Mater. 321 (1) (2003) 29–39.

[55] D. Michel, J. Moteff, A. Lovell, Substructure of type 316 stainless steel deformed in slow tension at temperatures between 21 and 816 °C, Acta Metall. 21 (9) (1973) 1269–1277.

[56] N. Nakada, H. Ito, Y. Matsuoka, T. Tsuchiyama, S. Takaki, Deformation-induced martensitic transformation behavior in cold-rolled and cold-drawn type 316 stainless steels, Acta Mater. 58 (3) (2010) 895–903.

[57] M. Multigner, S. Ferreira-Barragáns, E. Frutos, M. Jaafar, J. Ibáñez, P. Marín, M. Pérez-Prado, G. González-Doncel, A. Asenjo, J. González-Carrasco, Superficial severe plastic deformation of 316 LVM stainless steel through grit blasting: Effects on its microstructure and subsurface mechanical properties, Surf. Coat. Technol. 205 (7) (2010) 1830–1837.

[58] R. Chattopadhyay, Surface Wear: Analysis, Treatment, and Prevention, ASM International, 2001.

[59] T. Kosolapova, Carbides: Properties, Production, and Applications, Springer US, 2012.

[60] H. Pierson, Handbook of Refractory Carbides & Nitrides: Properties, Characteristics, Processing and Applications, Elsevier Science, 1996.

[61] M. Cuppari, S. Santos, Physical properties of the NbC carbide, Metals 6 (10) (2016) 250.

[62] C. Lin, C. Chang, J. Chen, W. Wu, Hardness, toughness and cracking systems of primary $(Cr,Fe)_{23}C_6$ and $(Cr,Fe)_7C_3$ carbides in high-carbon Cr-based alloys by indentation, Mater. Sci. Eng. A 527 (18–19) (2010) 5038–5043.

[63] P. Apps, J. Bowen, P. Prangnell, The effect of coarse second-phase particles on the rate of grain refinement during severe deformation processing, Acta Mater. 51 (10) (2003) 2811–2822.

[64] Y. Cao, S. Ni, X. Liao, M. Song, Y. Zhu, Structural evolutions of metallic materials processed by severe plastic deformation, Mater. Sci. Eng. R 133 (2018) 1–59.

[65] G. Olson, M. Cohen, A general mechanism of martensitic nucleation: Part I. General concepts and the FCC → HCP transformation, Metall. Trans. A 7 (12) (1976) 1897–1904.

[66] G. Olson, M. Cohen, A general mechanism of martensitic nucleation: Part II. FCC → BCC and other martensitic transformations, Metall. Trans. A 7 (12) (1976) 1905–1914.

[67] G. Olson, M. Cohen, A general mechanism of martensitic nucleation: Part III. Kinetics of martensitic nucleation, Metall. Trans. A 7 (12) (1976) 1915–1923.

[68] J. Venables, The martensite transformation in stainless steel, Philos. Mag.: J. Theor. Exp. Appl. Phys. 7 (73) (1962) 35–44.

[69] H. Fujita, S. Ueda, Stacking faults and fcc (γ) → hcp (ϵ) transformation in 188-type stainless steel, Acta Metall. 20 (5) (1972) 759–767.

[70] Z. Nishiyama, Martensitic Transformation, Elsevier, 2012.

[71] G. Olson, M. Cohen, A mechanism for the strain-induced nucleation of martensitic transformations, J. Less Common Metals 28 (1) (1972) 107–118.

[72] L. Murr, K. Staudhammer, S. Hecker, Effects of strain state and strain rate on deformation-induced transformation in 304 stainless steel: Part II. Microstructural study, Metall. Trans. A 13 (4) (1982) 627–635.

[73] S. Hecker, M. Stout, K. Staudhammer, J. Smith, Effects of strain state and strain rate on deformation-induced transformation in 304 stainless steel: Part I. Magnetic measurements and mechanical behavior, Metall. Trans. A 13 (4) (1982) 619–626.

[74] K. Staudhammer, L. Murr, S. Hecker, Nucleation and evolution of strain-induced martensitic (bcc) embryos and substructure in stainless steel: A transmission electron microscope study, Acta Metall. 31 (2) (1983) 267–274.

[75] G. Kang, Y. Dong, H. Wang, Y. Liu, X. Cheng, Dislocation evolution in 316L stainless steel subjected to uniaxial ratchetting deformation, Mater. Sci. Eng. A 527 (21–22) (2010) 5952–5961.

[76] C. Gaudin, X. Feaugas, Cyclic creep process in AISI 316L stainless steel in terms of dislocation patterns and internal stresses, Acta Mater. 52 (10) (2004) 3097–3110.

[77] X. Feaugas, On the origin of the tensile flow stress in the stainless steel AISI 316L at 300 K: Back stress and effective stress, Acta Mater. 47 (13) (1999) 3617–3632.

[78] S. Kang, J. Jung, M. Kang, W. Woo, Y. Lee, The effects of grain size on yielding, strain hardening, and mechanical twinning in Fe–18Mn–0.6c–1.5Al twinning-induced plasticity steel, Mater. Sci. Eng. A 652 (2016) 212–220.

[79] M. Pham, C. Solenthaler, K. Janssens, S. Holdsworth, Dislocation structure evolution and its effects on cyclic deformation response of AISI 316L stainless steel, Mater. Sci. Eng. A 528 (7–8) (2011) 3261–3269.

[80] K. Dutta, S. Sivaprasad, S. Tarafder, K. Ray, Influence of asymmetric cyclic loading on substructure formation and ratcheting fatigue behaviour of AISI 304LN stainless steel, Mater. Sci. Eng. A 527 (29–30) (2010) 7571–7579.

[81] Y. Dong, G. Kang, Y. Liu, H. Wang, X. Cheng, Dislocation evolution in 316 L stainless steel during multiaxial ratchetting deformation, Mater. Charact. 65 (2012) 62–72.

[82] A. Das, Cyclic plasticity induced transformation of austenitic stainless steels, Mater. Charact. 149 (2019) 1–25.

[83] Y. Li, D. Yu, B. Li, X. Chen, Martensitic transformation of an austenitic stainless steel under non-proportional cyclic loading, Int. J. Fatigue 124 (2019) 338–347.

[84] Q. Xue, E. Cerreta, G. Gray, Microstructural characteristics of post-shear localization in cold-rolled 316L stainless steel, Acta Mater. 55 (2) (2007) 691–704.

[85] Q. Xue, G. Gray, Development of adiabatic shear bands in annealed 316L stainless steel: Part I. Correlation between evolving microstructure and mechanical behavior, Metall. Mater. Trans. A 37 (8) (2006) 2435–2446.

[86] Q. Xue, G. Gray, Development of adiabatic shear bands in annealed 316L stainless steel: Part II. TEM studies of the evolution of microstructure during deformation localization, Metall. Mater. Trans. A 37 (8) (2006) 2447–2458.

[87] T. Nieh, J. Wadsworth, O. Sherby, Superplasticity in Metals and Ceramics, Cambridge University Press, 2005.

[88] M. Gutkin, I. Ovid'Ko, N. Skiba, Crossover from grain boundary sliding to rotational deformation in nanocrystalline materials, Acta Mater. 51 (14) (2003) 4059–4071.

[89] O. Kaibyshev, Superplasticity of Alloys, Intermetallides and Ceramics, Springer Science & Business Media, 1992.

[90] K. Huang, R. Logé, A review of dynamic recrystallization phenomena in metallic materials, Mater. Des. 111 (2016) 548–574.

[91] F. Humphreys, M. Hatherly, Recrystallization and Related Annealing Phenomena, Elsevier, 2012.

[92] D. Rigney, L. Chen, M. Naylor, A. Rosenfield, Wear processes in sliding systems, Wear 100 (1–3) (1984) 195–219.

[93] D. Rigney, Transfer, mixing and associated chemical and mechanical processes during the sliding of ductile materials, Wear 245 (1–2) (2000) 1–9.

[94] S. Kuo, D. Rigney, Sliding behavior of aluminum, Mater. Sci. Eng. A 157 (2) (1992) 131–143.

[95] P. Heilmann, J. Don, T. Sun, D. Rigney, W. Glaeser, Sliding wear and transfer, Wear 91 (2) (1983) 171–190.

[96] A. Smith, The friction and sliding wear of unlubricated 316 stainless steel at room temperature in air, Wear 96 (3) (1984) 301–318.

[97] Z. Yang, M. Naylor, D. Rigney, Sliding wear of 304 and 310 stainless steels, Wear 105 (1) (1985) 73–86.

[98] A. Alpas, H. Hu, J. Zhang, Plastic deformation and damage accumulation below the worn surfaces, Wear 162 (1993) 188–195.

[99] B. Hockenhull, E. Kopalinsky, P. Oxley, An investigation of the role of low cycle fatigue in producing surface damage in sliding metallic friction, Wear 148 (1) (1991) 135–146.

[100] J. Challen, P. Oxley, B. Hockenhull, Prediction of Archard's wear coefficient for metallic sliding friction assuming a low cycle fatigue wear mechanism, Wear 111 (3) (1986) 275–288.

[101] A. Kapoor, A re-evaluation of the life to rupture of ductile metals by cyclic plastic strain, Fatigue Fract. Eng. Mater. Struct. 17 (2) (1994) 201–219.

[102] A. Hearle, K. Johnson, Mode II stress intensity factors for a crack parallel to the surface of an elastic half-space subjected to a moving point load, J. Mech. Phys. Solids 33 (1) (1985) 61–81.

[103] A. Rosenfield, A fracture mechanics approach to wear, Wear 61 (1) (1980) 125–132.